

FULL PAPER

Open Access



# The spatial properties of the site amplifications of S-waves by generalized spectral inversion technique and the correction method of the site amplifications considering the contribution of later arrivals after major S-waves

Kenichi Nakano<sup>1\*</sup>  and Hiroshi Kawase<sup>2</sup>

## Abstract

Site amplification is an important component of strong ground motion prediction as it differs among sites, reflecting its specific local subsurface geology. Here, we confirm that site amplifications are similar in a neighborhood area over a long period. However, few studies have investigated the spatial properties in a wide region (i.e., the whole of Japan). In this study, we explored the spatial properties of site amplifications based on the generalized inversion technique (GIT) using Fourier amplitude spectra (FAS) as well as pseudo-velocity response spectra (pSv) as the latter is an important index for engineering purposes and the most similar type of response spectra to FAS. The spatial distributions of S-wave site amplifications (SA-S), especially within large sediment basins (e.g., the Kanto and Osaka Basins in Japan), were found to be relatively similar in proximate areas for a long period ranging from 2 to 8 s. This suggests that we could easily predict the site amplifications using an empirical approach through spatial interpolation based on the properties obtained by the GIT. Furthermore, we propose a prediction procedure for site amplification for the whole duration from the SA-S at an arbitrary site. We used the correction function, which converts the SA-S to the site amplification for the whole duration (SA-W), including an S-wave portion and a subsequent portion. This function is called the whole-duration to S-wave spectral ratio (WSR) and is stable in terms of spatial properties. As we could estimate the SA-S either by theoretical transfer functions or observed microtremors, we can easily predict the SA-W based on the proposed WSR concept. We found that SA-S in pSv is more or less similar to SA-S in FAS, however, SA-W in pSv fails to capture the effects of the long duration of ground motions inside a large basin so that we cannot recommend to use pSv for the prediction of whole duration of ground motion.

**Keywords** Generalized inversion technique, Pseudo-velocity response spectra, Fourier amplitude, Site amplification, Spatial distribution, WSR

\*Correspondence:

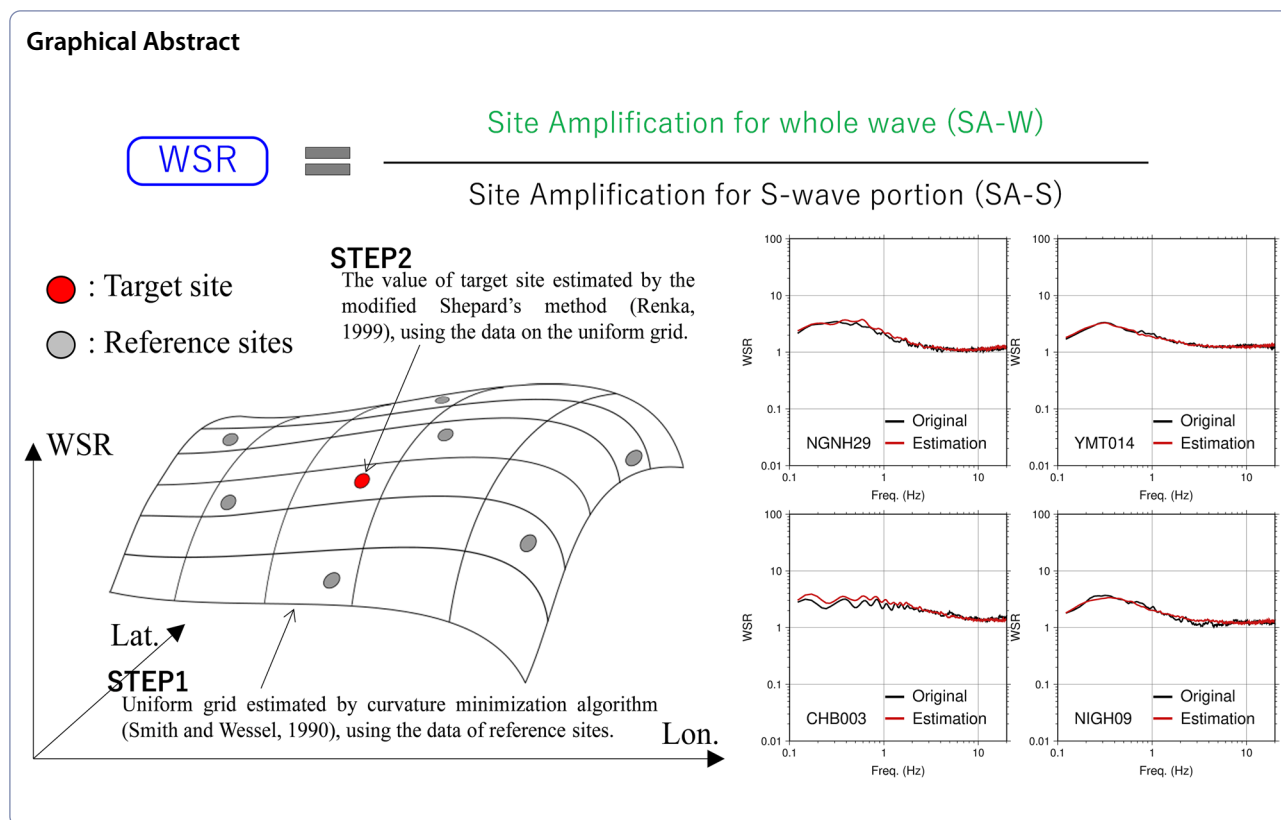
Kenichi Nakano

nakano.kenichi@ad-hzm.co.jp

Full list of author information is available at the end of the article



© The Author(s) 2023. **Open Access** This article is licensed under a Creative Commons Attribution 4.0 International License, which permits use, sharing, adaptation, distribution and reproduction in any medium or format, as long as you give appropriate credit to the original author(s) and the source, provide a link to the Creative Commons licence, and indicate if changes were made. The images or other third party material in this article are included in the article's Creative Commons licence, unless indicated otherwise in a credit line to the material. If material is not included in the article's Creative Commons licence and your intended use is not permitted by statutory regulation or exceeds the permitted use, you will need to obtain permission directly from the copyright holder. To view a copy of this licence, visit <http://creativecommons.org/licenses/by/4.0/>.



**Introduction**

To predict strong ground motions for engineering purposes, three fundamental characteristics need to be studied, namely source, path, and site amplification factors, and a model based on these characteristics needs to be constructed to precisely predict ground motions at a target site. There are two approaches for predicting the spectral shapes of strong ground motions. The first approach involves constructing regression analytical models based on the pseudo-velocity response spectra (pSv) or the pseudo-acceleration response spectra (pSa). A response spectrum is generally used to grasp the seismic response of a structure as a single degree-of-freedom system (SDOF) at different predominant periods. This approach/model is widely accepted and has been termed the ground motion prediction equation (GMPE) or the ground motion model.

The other approach for predicting the spectral shapes of strong motions involves studying three fundamental characteristics using the generalized spectral inversion technique (GIT). This technique helps to estimate the physical parameters controlling the mechanisms considered in generating ground motions and reconstruct precise models based on Fourier amplitude spectra (FAS). These characteristics can also be used to

generate an elemental wave for the statistical Green's function method (e.g., Nakano and Kawase 2021a).

As the building code in Japan has been adapted to account for procedures that compute the ground motions, with an amplitude designed to satisfy pSv from the acceleration response spectra with 5% damping, it is common to predict strong motions using pseudo-response spectra (or normal response spectra) to reflect the characteristics in the seismic design of buildings. There are studies of the three fundamental characteristics (source, pass, and site) that were conducted via pseudo-response spectra based on regression analysis in the empirical approach (e.g., Kataoka et al. 2006; Satoh et al. 2010; Abrahamson et al. 2008; Bozorgnia et al. 2014). These studies have mainly focused on the application of GMPEs. Satoh et al. (1998) pointed out that the shapes of the site amplification coefficients evaluated in GMPEs with pSv were similar to those estimated by Fourier spectra in the frequency domain, although the coefficients of pSv and Fourier spectra were different owing to their different physical backgrounds, as shown by Bora et al. (2016). However, as an engineering requirement for the design of a structure, we only need the precise pSv (or seismic waveforms), which is estimated via the source, path, and site coefficients at a

target site. For this purpose, it is beneficial to study the properties of these coefficients separately from the absolute value of the observed  $pSv$ , even though  $pSv$  has only the maximum value of the response of an SDOF system to ground motion. In some cases, such a representation is called a partially non-ergodic GMPE (e.g., Abrahamson et al. 2019) as the site-specific approach works well in reducing the variabilities in GMPEs. Notably, the GIT for response spectra can be considered as a similar analysis procedure to the first-step regression (for event-specific decomposition) in the two-step regression analysis of the GMPE (e.g., Joyner and Boore 1981, 1993; Fukushima and Tanaka 1990). A big difference between GIT and the two-step regression is that the former usually uses a non-parametric inversion but the latter uses a regression with fixed parameters such as a magnitude for a source term. This kind of investigation on GMPE as well as GIT for both the absolute acceleration response spectra (SA) and FAS has been performed by Bindi et al. (2017).

In the previous studies several researchers performed the direct comparison of FAS and SA as Bindi et al. (2017) did or FAS and  $pSa$  as Montejo and Vidot-Vega (2017) did, and found common monotonically increasing trends between them because of their different physical backgrounds. We selected  $pSv$  here because theoretically  $pSv$  coincides with the acceleration FAS if we measure  $pSv$  at the end of the input motion and if the damping used is zero (e.g., Hudson 1962). Of course, maximum response would rarely occur at the end of input motions and we use 5% damping to calculate  $pSv$ , yet this fundamental physical relationship between  $pSv$  and FAS seems sufficient for us to select  $pSv$  for GIT, rather than the SA or  $pSa$ .

However, the separation of source, path, and site terms from the observed ground motions would only be meaningful for Fourier spectra as the physical source, path, and site terms are connected in the form of convolutions, independently for each frequency. For this reason, the GIT for FAS was used as early as in the 1980s in the pioneering work of Andrews (1982). In the GIT analysis, each term in the FAS has a distinctive physical meaning. An important aspect of the GIT analysis is the choice of the reference, which is needed as an a priori constraint in the separation of source, path, and site contributions to ground motions. Andrews (1982) used no site-specific site-term assumption, leading to the contamination of the site-term into the source and/or attenuation terms. Under this assumption, with a sufficient number of event–site pairs, the average site amplification of all sites used will be primarily transferred to the source term. If the exact source spectrum of one specific event is known, it can be used as a reference; however, this is highly unlikely without making some specific assumptions.

In our analyses (e.g., Kawase and Matsuo 2004; Kawase 2006; Nakano et al. 2015, 2019; Nakano and Kawase 2019, 2021a, 2021b), we used one rock site (i.e., the reference site) from which we extracted the local site amplification by the weathered rock formations to obtain the seismological bedrock spectra as a constraint to evaluate the three fundamental factors.

In this study, we focused on site-specific site amplifications (relative to seismological bedrock) as site amplification is a dominant characteristic in strong-motion predictions at an arbitrary site. We estimated both site factors in  $pSv$  and FAS.

For strong-motion predictions, we need to obtain a precise site amplification factor at the target site, which required numerical computation or an empirical method. Unfortunately, the identification of the site amplification term at the target site by numerical computation is challenging, as this requires information on the soil properties from the shallow part of a subsurface structure down to the seismological bedrock; and acquiring this without sufficient time and funds in advance, is difficult. It is even more difficult to simultaneously predict strong motions at many sites. Senna et al. (2013) and Wakai et al. (2019) compiled a large amount of observed data and proposed a subsurface structure model that combined a part model that is shallower than the engineering bedrock, with a spatial resolution of approximately 250 m, and a part model that is deeper than the engineering bedrock, with a spatial resolution of approximately 1 km, in the Kanto and Tokai regions in Japan. Although so far, this is the most precise velocity model for Japan, one-dimensional ground response analysis at only 40% of the strong motion observation sites can successfully reproduce empirically obtained site factors (e.g., Ito et al. 2021).

For the latter (that is, an empirical method), numerous empirical methods for the prediction of site-specific site amplifications have been proposed since the early 1970s, but no final solution has been obtained. However, if we could precisely estimate the site amplification at arbitrary sites based on a simple empirical approach, such as spatial interpolation without an invasive boring survey or non-invasive exploration methods, we could rapidly and precisely predict strong motions at a target site and/or many target sites. We believe that the spatial distribution and properties of the site amplifications mentioned below provide clues for future strong-motion predictions.

We focused not only on the site amplifications evaluated by the GIT directly for an S-wave portion of strong motions, but also on the site characteristics estimated for the whole duration, including an S-wave portion and a subsequent portion (e.g., Nakano et al. 2019; Nakano and Kawase 2019, 2021a, 2021b). In our previous studies (e.g., Nakano 2020; Nakano and Kawase 2021a, 2021b),

we found that the ratio of site amplifications, which were calculated as the ratio of the site amplification for the whole duration including an S-wave portion and a subsequent portion relative to the site amplification only for the S-wave portion, is large (around 10) in the frequency range lower than 2–3 Hz at sites inside large sedimentary basins but small in the frequency range above 3 Hz. For sites outside the sedimentary basins, the ratio is quite small ( $<2$ ) for the entire frequency range. We named this spectral ratio whole-duration to S-wave portion spectral ratio (WSR). It should be noted that WSRs are similar to each other within vicinity sites inside the same basin as it primarily reflects the contributions of the basin-induced surface waves in the later part of ground motion, which is controlled by the whole basin structure, not a structure immediately below the site. Thus, it largely contributes to the low-frequency ground motion characteristics at sites in sedimentary basins (e.g., Bard and Bouchon 1980a; 1980b; Kawase and Aki 1989; Kawase 1993). As shown below, the WSR for pSv tends to be negligible because of the saturation characteristics of pSv as to the long duration.

Here, we report an analysis to investigate the spatial properties of site amplification factors based on the GIT, using not only Fourier spectra but also pSv. We also investigated the spatial distributions of the site amplification factors estimated by the GIT, using Fourier amplitude spectra and pSv. We estimated WSRs at observation sites that were targeted in our previous studies (e.g., Nakano et al. 2015, 2019; Nakano and Kawase 2019, 2021a, 2021b) from the ratio of the site amplification evaluated by the S-wave portion of strong motions and the whole duration, including an S-wave and subsequent portions. We also estimated dense spatial distributions of WSRs in the frequency domain, and based on these, we constructed an interpolated model of the WSRs to estimate the spatial distribution on arbitrary sites. Furthermore, we proposed a correction method for the site amplification factors, considering the contribution of subsequent portions based on WSR, to precisely predict the site amplification with the whole duration at arbitrary sites. Finally, we checked the usability of the proposed method by reproducing WSRs and confirmed their efficacy by checking the correlation and residuals with respect to the original data.

## Dataset and method

### Dataset

Nakano et al. (2015) constructed a dataset of strong-motion records in Japan to perform a GIT analysis to evaluate the characteristics of the source, path, and site. They collected strong-motion records published by K-NET, KiK-net, and the JMA Shindo-kei network

(JMA95), all of which had been deployed all over Japan. Both K-NET and KiK-net are operated by the National Research Institute for Earth Science and Disaster Resilience (NIED 2019). These networks immediately provide strong-motion records through their webpages soon after an earthquake occurs. The JMA Shindo-kei network (e.g., Kodera et al. 2018) is operated by the Japan Meteorological Agency to announce the JMA seismic intensity after an earthquake as quickly as possible. Strong-motion records were provided by the Japan Meteorological Business Support Center (JMBSC).

In this study, we added new strong-motion records of JMA87, JMA95, K-NET, KiK-net, and CEORKA (The Committee of Earthquake Observation and Research in the Kansai Area) to the dataset constructed previously by Nakano et al. (2015) and reconstructed the dataset from August 1988 to June 2019. However, after January 2017, we only included records of several damaging earthquakes. We selected records with JMA magnitude  $M_{\text{JMA}} \geq 4.5$  and hypocentral depth  $\leq 60$  km. For the JMA95 type, we used only the records between 2012 and 2016, which were scrutinized and corrected by the JMA for some errors in the records. Hereafter, we refer to the observation sites published by the JMA as the “JMA\_XXX”, where “XXX” represents each site code defined by the JMA. We considered the relocation of the observation site in K-NET and subsequently renamed the relocated site in K-NET by adding 100 on the three digit numbers after the fourth character in the original site codes, excluding the sites in Hokkaido Prefecture in Japan. (In the case of Hokkaido Prefecture, we added 200 instead of 100, because the total number of observation sites exceeds 100.)

Figure 1 shows the seismic observation points, segmented area, and locations of the epicenters with the focal depth to consider the regional characteristics. The segmented area was adopted based on the criteria defined by Nakano et al. (2015). We classified the earthquakes, represented in panels (b)–(d), into the following types: Type B (plate-boundary earthquakes), Type I (intraplate earthquakes), and Type C (crustal earthquakes). We extracted a portion of the waves after the onset of S-wave arrival, using the following criteria: 5 s for  $M_{\text{JMA}} \leq 6$ , 10 s for  $6 < M_{\text{JMA}} \leq 7$ , and 15 s for  $7 < M_{\text{JMA}}$ . We also added a 2 s cosine taper to the start and end-portions of the extracted waveforms and padded with zero to obtain a duration of 40.96 s. The window sizes of S-wave used here are rather short because we would like to extract only the S-wave dominant part to make separation as close as possible to the physical formula of GIT. As a compensation, we are sacrificing the inclusion of the whole low-frequency energy. We switched the JMA’s travel-time tables (e.g., Ueno

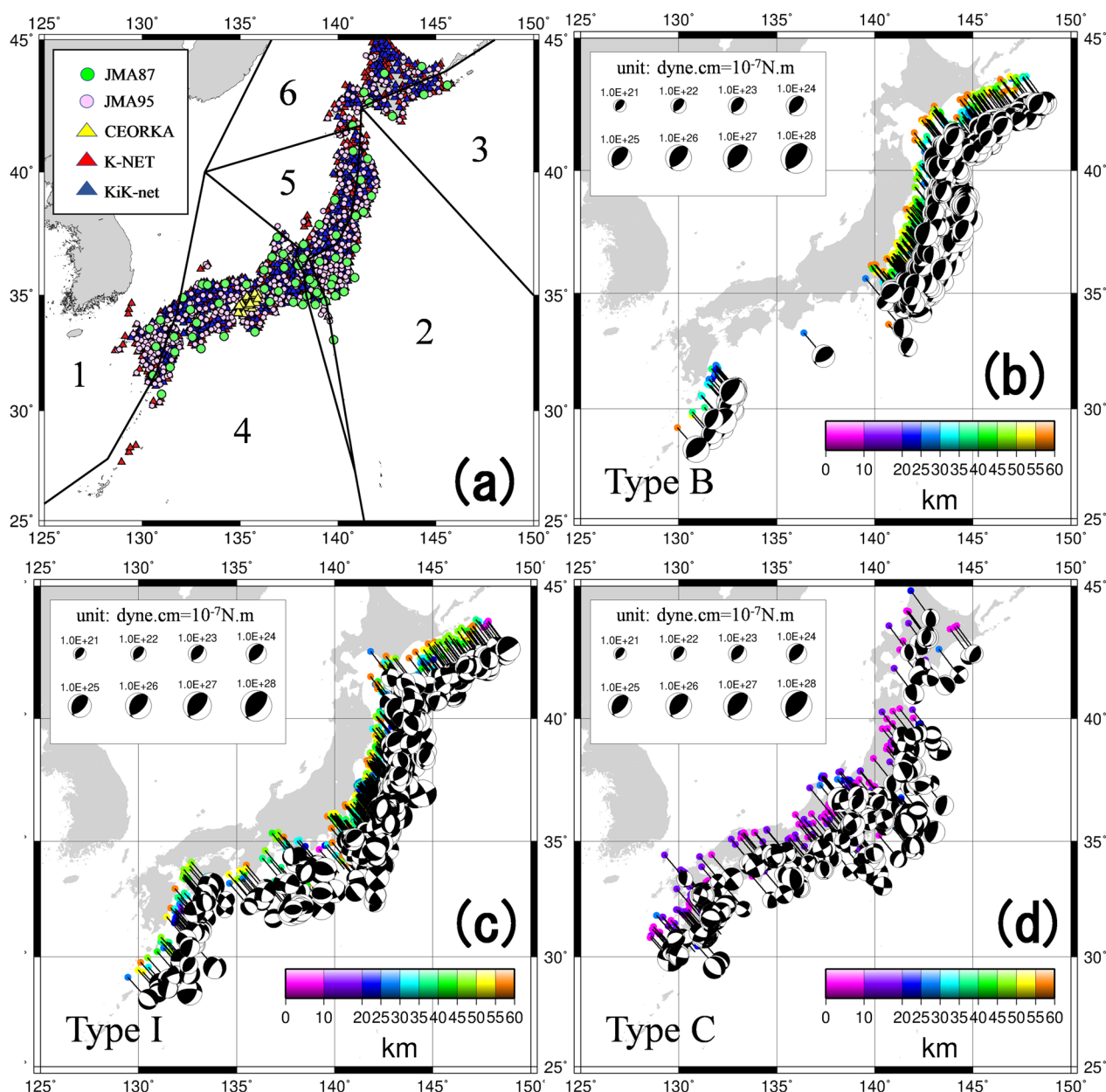


**Fig. 1** a Observation points in strong-motion observation networks in Japan; b fault mechanisms for boundary-plate earthquakes with color-coded focal depth information; c fault mechanisms for intraplate earthquakes; d fault mechanisms for crustal earthquakes

et al. 2002) based on the earthquake occurrence date because we wanted to use the same travel-time tables for the origin time and hypocenter determination at the time of occurrence for consistency. Dataset details and the treatment of waveforms, can be accessed from our previous work (e.g., Nakano et al. 2015; Nakano and Kawase 2019; Nakano 2020). The number of strong-motion records in the dataset was 451,404 (e.g., Nakano 2020). We discussed the effects of the nonlinear soil response that might affect the dataset according to the

selection condition of the waves in terms of the peak ground acceleration (PGA) in our previous study (e.g., Nakano and Kawase 2019). Since then, we have been studying the deviation of earthquake horizontal-to-vertical spectral ratios (eHVSr) as a function of PGAs to delineate the nonlinear effects (e.g., Wang et al. 2021) and found that small deviations in eHVSr will appear at certain sites with PGAs as minor as 100 cm/s<sup>2</sup>. However, as long as we restrict ourselves to using data with

a PGA less than 200 cm/s<sup>2</sup>, the effects of nonlinearity would not be significant.

#### Analysis based on the spectral inversion technique

We performed the GIT to separate the source, path, and site terms from the strong-motion records in the dataset established in the previous section. Here, for both the FAS and pSv, corresponding to the S-wave portion of the waveforms, we used formularization using the S-wave far-field approximation directly from the source to the site, as shown in Eqs. (1)–(4):

$$F_{S-ij}(f) = S_i(f) \cdot P_{ij}(f) \cdot G_{S-j}(f), \quad (1)$$

$$\log_{10} F_{S-ij}(f) = \log_{10} S_i(f) + \log_{10} P_{ij}(f) + \log_{10} G_{S-j}(f), \quad (2)$$

$$\log_{10} P_{ij}(f) = -n_{l(i)}(f) + \sum_k b_{l(i)k}(f) \cdot X_{ijk}, \quad (3)$$

$$X_{ij} = \sum_k X_{ijk}, \quad (4)$$

where  $F_{S-ij}$  is the FAS or pSv of the S-wave portion,  $S_i$  is the  $i$ th source characteristic,  $G_{S-j}$  is the site amplification directly estimated by the GIT using the S-wave portion (SA-S) for the  $j$ th observation point, and  $P_{ij}$  is the attenuation characteristic defined by Eq. (3) along the line from the  $i$ th source location to the  $j$ th observation point. The  $n$  represents the geometric attenuation, which is assumed to be 1.0 until  $X_{ij}$  is less than 100 km, then we invert  $n$  for each frequency to take the Moho and other interface reflections into account. In Eq. (3),  $b$  represents a combination of intrinsic and scattering attenuation. As we focused on the regional differences in attenuation characteristics, the attenuation term  $b$  was chosen based on six regions (where  $k$  is the index for regions), including quaternary period volcanic fronts and the Itoigawa–Shizuoka Tectonic Line (ISTL) as their boundaries. The term  $l(i)$  represents the type of the  $i$ th earthquake. The term  $X_{ij}$  multiplied by the attenuation term is the hypocentral distance, with  $X_{ijk}$  representing the apparent distance passing through region  $k$  (which is determined by the distribution of the horizontal distance passing through a specific region  $k$  along the direct path). We evaluated the unknown parameters of Eqs. (2) and (3) based on the dataset including the new records mentioned above. In this study, we used the root-mean-square values of the two horizontal components of FAS or pSv.

We used accelerograms observed at K-NET and KiK-net, CEORKA, JMA 87-type electromagnetic strong-motion seismographs, and JMA 95-type seismic intensity meters (i.e., the JMA Shindo-kei network). The

data must satisfy the following conditions: hypocentral distance  $\leq 200$  km,  $0.2 \text{ cm/s}^2 \leq \text{PGA} \leq 200 \text{ cm/s}^2$ , and the number of sites uniquely identifying an earthquake  $\geq 3$ . We selected the reference site, YMGH01, located in Yamaguchi Prefecture in Japan, as a constraint condition to solve Eq. (2) as an adequate velocity structure model (i.e.,  $V_s$  profile) was already constructed by Kawase and Matsuo (2004) in YMGH01, from which we can extract the effects of weathered layers. The site amplification factors at the other sites were obtained as values normalized to this reference outcrop motion at YMGH01. However, bedrock S-wave velocity at YMGH01 was 3450 m/s; therefore, the resultant site amplification factors at the other sites could be regarded as absolute amplification values from the seismological bedrock. Please see our previous studies for details of deconvolution analysis (e.g., Kawase and Matsuo 2004; Nakano et al. 2015).

#### Definition of site amplification

After performing the GIT for the S-wave portion, site amplifications with the whole wave for the whole durations of earthquake motions (SA-S and site amplification with the subsequent portion including the whole wave; SA-W) were separately evaluated as described by Nakano and Kawase (2019). We first estimated the source spectrum, propagation characteristics, and site characteristics using the GIT with the FAS of the S-wave portion in the waveforms. Note that the S-wave portion in the waveform was identified automatically by the observed time in the strong-motion records and the occurrence time of each event. We calculated the arrival time of the S-wave at each observation site with the hypocentral distances of the source location in each event based on the JMA's travel-time table (e.g., Ueno et al. 2002). By using the spectrum without the site term calculated from the separated source and attenuation terms for a specific site from a specific event and the FAS for a whole duration of wave, we could derive the site amplification for a whole wave. The logarithmic averaging operation of the site amplifications of individual earthquakes evaluated at a specific site yielded the SA-W at that site. It should be noted that SA-W is relative to the seismological bedrock motion of the incoming S-wave, and thus, it is always equal to or higher than the site amplification factors with the S-wave, that is, SA-S.

The SA-W was calculated using Eq. (5):

$$G_{W-j}(f) = \langle F_{W-ij}(f) / (S_i(f) \cdot P_{ij}(f)) \rangle, \quad (5)$$

where  $G_{W-j}$  is the SA-W at the  $j$ th site,  $F_{W-ij}$  is the FAS or pSv of the ground motion with the whole duration observed at the  $j$ th site in  $i$ th earthquake,  $S_i$  is the S-wave

source term separated by the GIT,  $P_{ij}$  is the S-wave attenuation term between the source point in  $i$ th earthquake and the observation point at the  $j$ th site. The brackets  $\langle \rangle$  represent the operation of averaging with the logarithm of the spectra observed at the  $j$ th site.

Figure 2a shows a conceptual diagram of SA-S and SA-W, as defined above. In the figure, considering a case where the S-wave emitted from a point source is emerging vertically immediately beneath a site within the basin, we show the SA-S evaluated directly by the GIT. The SA-W is also indicated, considering the effects of basin-induced surface waves caused by the arrival of S-waves at the basin edge as well as multiply reflected S-waves inside the basin. In our analysis, all contributions of S-waves scattered outside the basin that arrived later than the S-wave window (i.e., S-coda) were included in the SA-W, not in the SA-S. We showed the different types of velocity waveforms observed at the site near the mountain and in the Kanto Basin, which were named GNM003 and TKY015 in K-NET (the locations are described below), in Panels (b)–(d) in Fig. 2. We selected the waveforms observed at GNM003 and TKY015 in the 2004 mid-Niigata earthquake, similar to Furumura et al. (2014). As shown in Panel (b), considerable long-period components appeared in the subsequent portion at TKY015, whereas there was no similar feature at GNM003. These differences appeared in the comparison of the FAS, as shown in Panel (c). As you can see, the amplitudes in the high-frequency domain higher than approximately 1 Hz at TKY015 are reduced. We think that it comes from the damping effects inside the deep sedimentary layers in the Kanto Basin. In Panel (d), we showed the locations of the sites (GNM003 and TKY015) with the seismological bedrock depth published by HERP (2012). According to Eq. (5), this kind of difference is directly reflected in the SA-W. In the simulations, the same features were reported in a previous study (e.g., Dhakal et al. 2011).

For the SA-W, we assumed that (1) all subsequent motions can be evaluated as an additional amplification on top of the reverberated S-wave coming directly below the site and (2) the propagation characteristics (i.e., attenuation by distance) of the wave that causes additional amplification within the basin (from the edge

of the basin to the target site) are the same as those of the direct S-wave propagating below the seismological bedrock. Therefore, the difference between the propagation characteristics of direct S-waves propagating below the basin from the epicenter to an observation point and those of various waves propagating inside the basin from the basin edge were also included in the SA-W.

### Comparison of site amplifications

According to the procedures described in the previous sections, the site amplifications of the SA-S were evaluated by the GIT directly, and those of the SA-W were re-calculated using the procedure mentioned above (e.g., Nakano and Kawase 2019; Nakano et al. 2019).

Figure 3 shows SA-S and SA-W values evaluated by the GIT from weak motions, with  $PGA \leq 200 \text{ cm/s}^2$  at sites as examples in Japan. The geometric means and means  $\pm 1\sigma$  of SA-W and the geometric means of SA-S are shown in red and black lines, respectively. The red lines are higher than the black lines in the low-frequency range, approximately lower than 2 Hz, whereas the red and black lines are close to each other in the high-frequency range, which is approximately above 2 Hz. The amount of additional amplification in the SA-W relative to the SA-S depends on the site; OSKH02, AIC003, KNG001, KNG002, JMA\_E4E, and TKY007 showed substantial additional amplifications, whereas KMMH16, ISK005, and SZO024 showed marginal differences. Among the different contributions to these differences, the major one would come from the basin-induced surface waves, which effectively prolong the duration of the strong motions because of the whole-basin propagations (e.g., Bard and Bouchon 1980a; b; Kawase and Aki 1989). In this context, the basin effects along with the locations of the sites need to be discussed in more detail. The  $T_z$  is defined as the travel-time of the S-wave in the sedimentary layers of the subsurface structure from the layer such as seismological bedrock (we choose the layer whose  $V_s$  reached 3.2 km/s) to the top layer based on JIVSM, published by HERP (2012). The  $AVS_z$  is defined as the average velocity of the S-wave from the layer as seismological bedrock to the top layer in the same manner as mentioned above, using  $T_z$  and the thickness of the layers

(See figure on next page.)

**Fig. 2 a** Illustration of the site amplification factors defined in this study. ‘SA-S’ shows the site amplification factor evaluated from the S-wave portion of the strong-motion records. ‘SA-W’ shows the site amplification factor evaluated from the whole duration of strong-motion records including both S-wave portion and the basin-induced surface-wave contributions (that comes after the S-wave). Note that we call the portion including the S-wave and surface-wave (as well as S-coda) “the whole wave” in this paper. **b** The velocity waveforms observed at GNM003 and TKY015 on K-NET in Japan (the location of these site is shown in Panel (d) in this figure mentioned later). **c** The Fourier amplitude spectra of the waveforms observed at GNM003 and TKY015 on K-NET in Japan we mentioned above are shown in this panel. The black lines represent the waveforms observed at GNM003, the red ones represent the waveforms observed at TKY015. **d** The locations of GNM003 and TKY015 with the seismological bedrock-depth published by HERP (we explained it in detail later) are shown in this panel

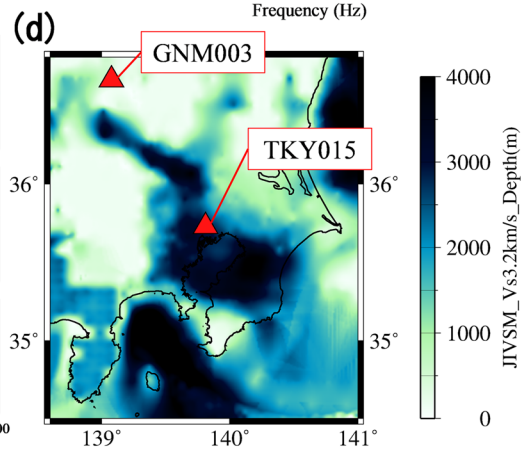
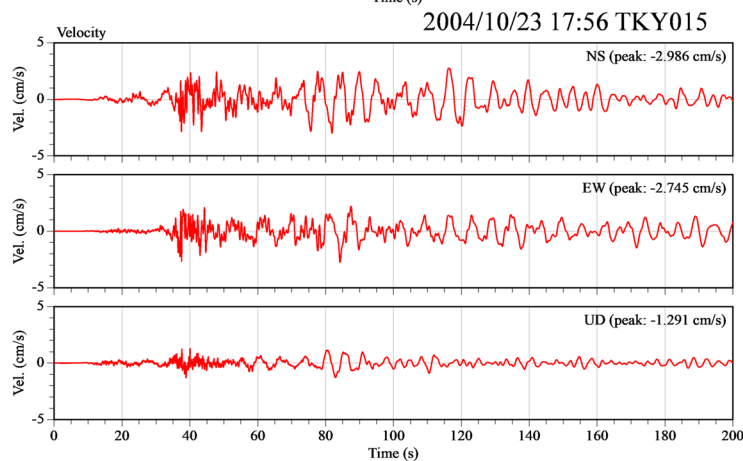
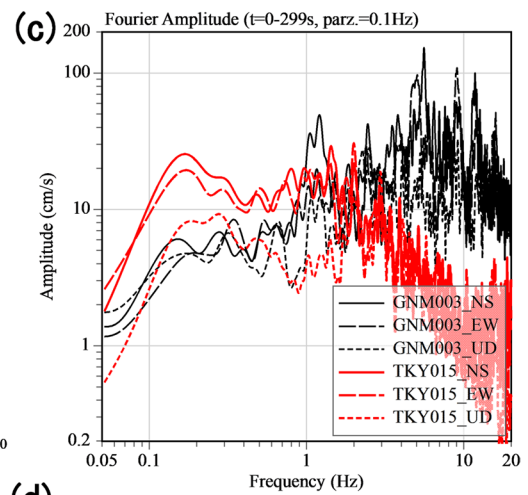
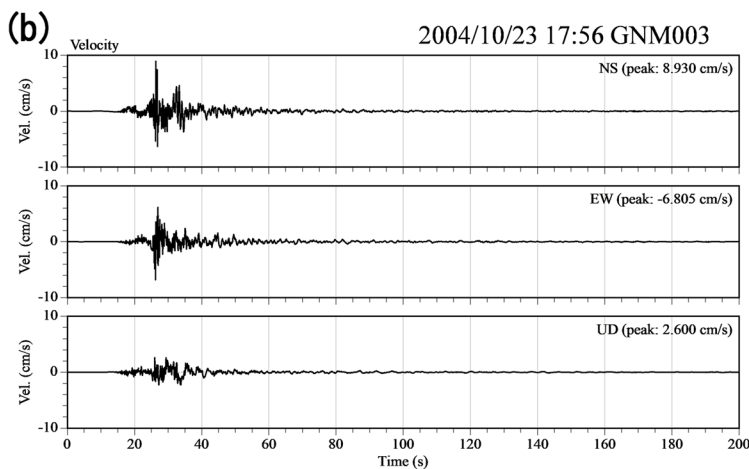
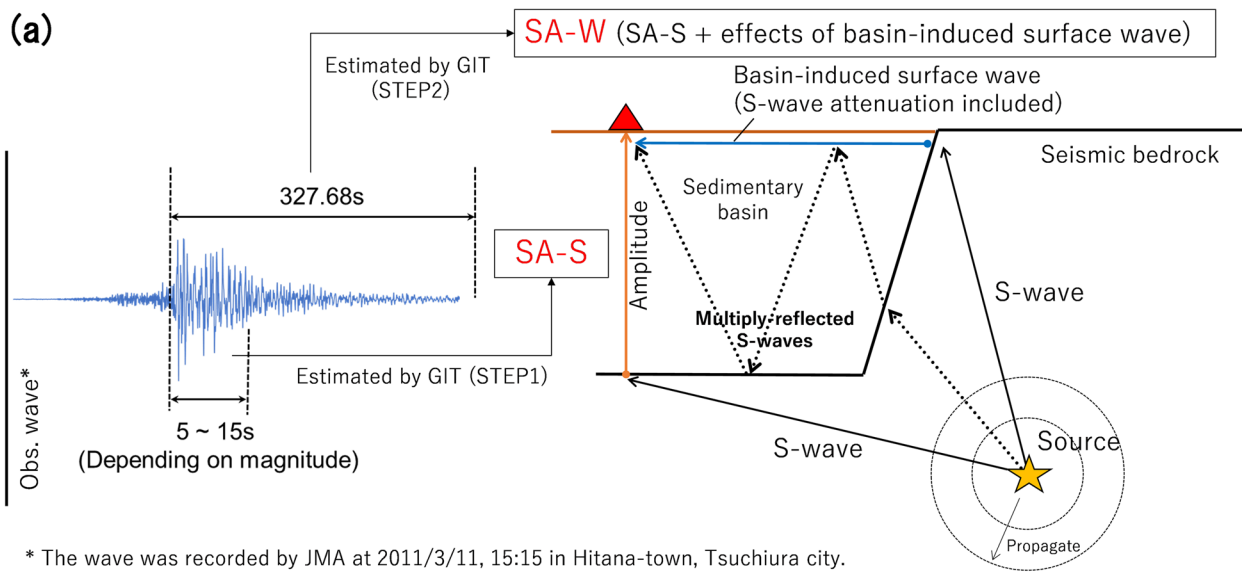


**Fig. 2** (See legend on previous page.)

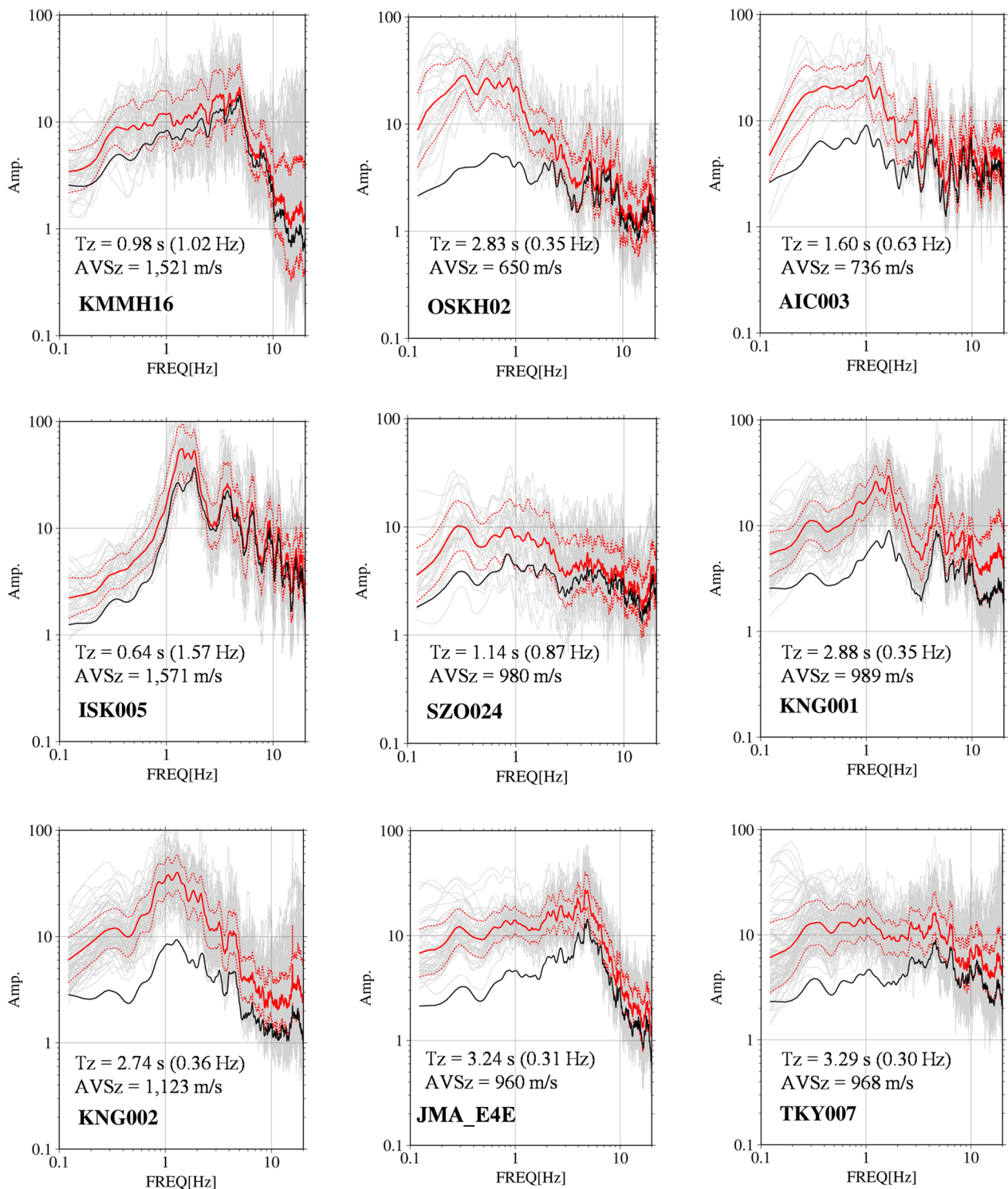


**Fig. 3** The site amplifications with S-waves and whole waves based on Fourier spectra. Black lines represent the site amplification evaluated by GiT directly, using the S-wave portion of the strong-motion records. Red lines represent the site amplification calculated as shown in Fig. 1, using the S-wave and coda-wave portion (i.e., whole duration after arrived S-wave) of the strong-motion records (Bold line is average; Thin line is average  $\pm 1\sigma$ ). In each graph, the solid red line indicates the geometrical mean value of the site amplification with whole wave (SA-W), the dotted red line indicates the mean value  $\pm 1\sigma$  (one standard deviation) of the SA-W calculated from site amplifications of individual records shown in gray lines, and the solid black line indicates the SA-S

in JIVSM. Both  $T_z$  and  $AVS_z$  are indicated in Fig. 3. The three sites (KMMH16, ISK005, and SZO024) are classified as the group with  $AVS_z \geq 1$  km/s and  $T_z \sim 1$  s or less. These sites are located in regions where no sedimentary basin exists or the size of the sedimentary basin is smaller than those of the Kanto Basin (i.e., TKY007, KNG001, KNG002, JMA\_E4E), the Nobi Basin (AIC003), and the Osaka Basin (OSKH02). We thus assume that the performance generating the basin-induced surface waves are relatively weak at these three sites outside of the sedimentary basins. We believe that this discussion provides a deeper understanding of basin-induced surface waves. However, a detailed investigation should be performed to quantify the source of these additional amplifications in the SA-W, which is beyond the scope of this article.

One may wonder why a two-step analysis is needed to obtain both SA-S and SA-W. Using Fourier spectra for the observed whole wave records for the GIT analysis directly would result in a negative  $Q$  problem in the lower frequency range. Under many circumstances, we may have sites with larger amplitudes inside a basin, whereas we may have sites with smaller amplitudes outside a basin, which could be closer to the source. If this type of situation (i.e., distant sites would have larger amplitudes) was dominant, only negative  $Q$ -values would fit the model to the data. When focusing on the S-wave portion, such an inversion of the amplitude with distance would not be substantial. However, when using whole-wave records for the GIT analysis, the effects of duration at sites inside a basin in the Fourier spectra are so strong that we cannot effectively separate the path and site terms.

Figure 4 shows the SA-S and SA-W values estimated by the GIT based on the pSv of the strong-motion records, following the procedure for FAS. The overall spectral shapes of the SA-S estimated for pSv and FAS are similar; however, the frequency fluctuations of the shapes of the site amplifications for pSv are much smoother than those for FAS. Owing to this strong smoothing effect, the peak amplitudes of the site amplification for pSv were much smaller than those for the Fourier spectra. We also note that the low-frequency decay in pSv is not apparent (close to flat), whereas a decaying tendency in the FAS can be seen clearly. These results reflect the fundamental characteristics of the physical meaning of pSv shown in Bora et al. (2016) and support the results reported in a previous study (e.g., Satoh et al. 1998).

As pSv is the maximum response value for a single-degree-of-freedom system with a natural frequency  $f_0$  and a 5% damping; therefore, the subsequent portion coming after the S-wave (i.e., coda waves and basin-induced surface waves) in the strong motions does not

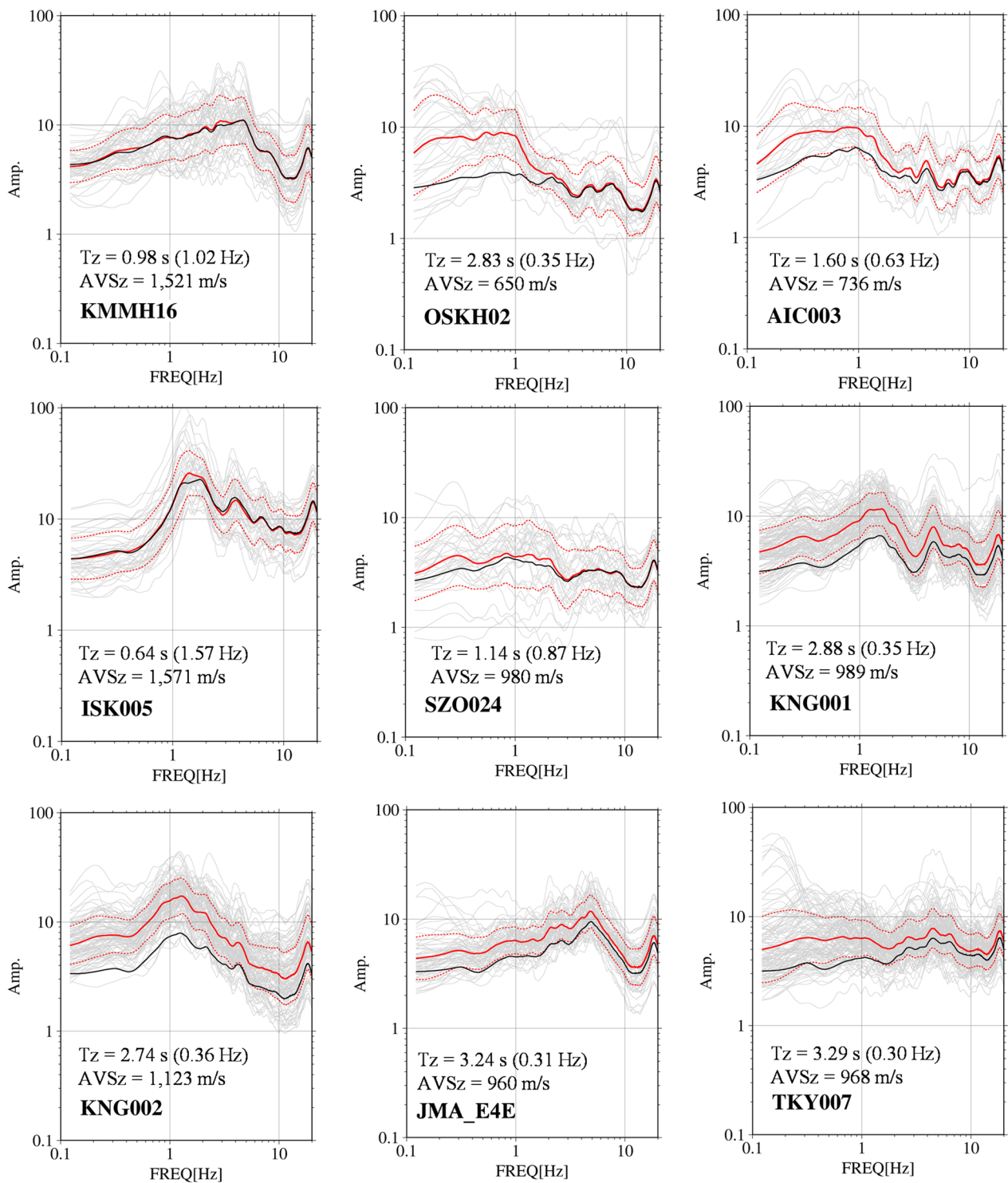
substantially contribute to the amplitude of pSv. The differences between the SA-S and SA-W estimated for pSv are smaller compared to the differences for FAS. For example, at sites with large differences, such as OSKH02, AIC003, KNG001, KNG002, JMA\_E4E, and TKY007, there were only two to three times of additional amplifications in pSv. These ratios were much smaller than the difference in the Fourier spectra, as shown in Fig. 3. At sites with fewer differences, such as KMMH16, ISK005, and SZO024, the SA-W was almost the same as the SA-S. These small differences between SA-S and SA-W are a direct consequence of the insensitivity of pSv to the duration of motion. In contrast, the FAS can correctly reflect the effect of the duration of the observed strong motions. Therefore, careful consideration of site amplifications to reflect the effect of duration so as to construct a ground motion prediction method based on the response spectra, is required. Owing to this insensitivity of pSv to duration, one-step GIT for the whole duration can be applied, as in the previous GMPE studies on pSv.

### Spatial distribution of the site amplifications

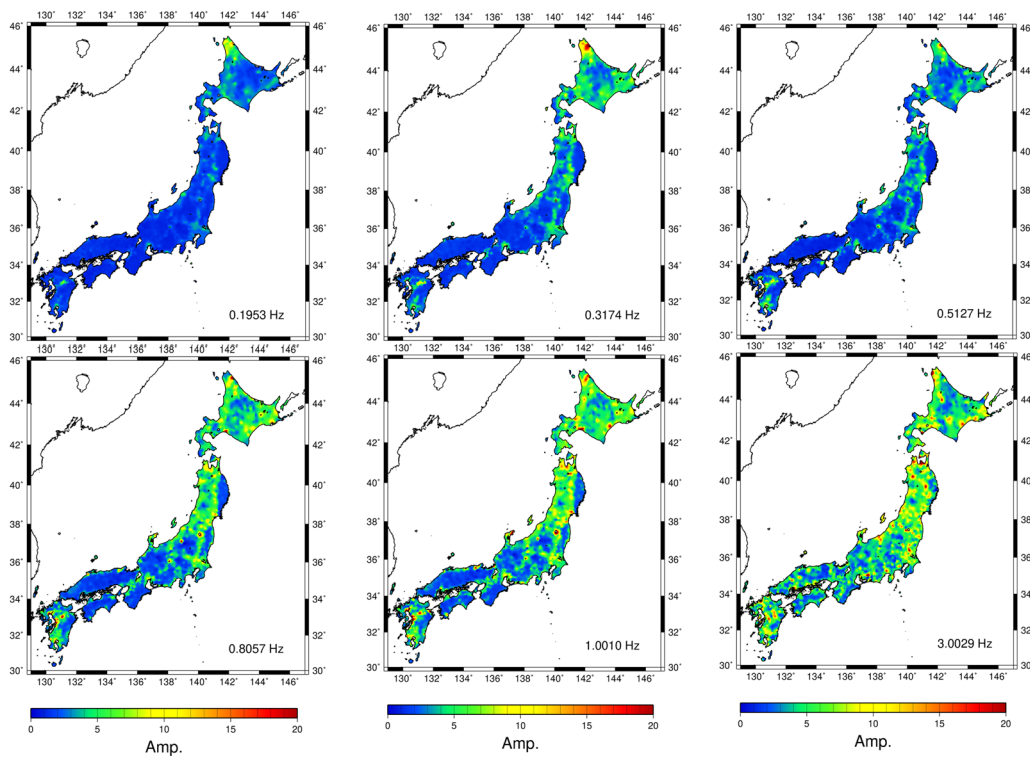
We show the spatial distribution based on the SA-S and SA-W evaluated in the previous section. We used the minimum curvature method (e.g., Smith and Wessel 1990) to interpolate the discrete data, namely site amplification, by grid points with a 3-km mesh covering all land regions in Japan.

Figure 5 shows the spatial distribution of the site amplifications estimated directly by GIT with the S-wave portion of the strong-motion records for FAS and pSv at six selected frequencies. In the figure, the color contour shows the amplitude of the site amplifications, where the warm color represents a high amplitude and the cold color a low amplitude. Figure 5 shows the smoothly varying distribution of high-amplitude areas at a frequency of less than approximately 1 Hz. These areas correspond to the regions where the seismological bedrock depths published by J-SHIS and the ones with the S-wave velocity  $V_s = 3.2$  km/s, based on the JIVSM published by HERP (2012), are relatively deep, as shown in Fig. 6. Because of this good correlation of SA-S in the low-frequency range with the depth of the seismological bedrock, we can expect to have a good prediction of SA-S if we simply interpolate SA-S of nearby sites as long as we have several sites within a small area ( $\sim 5$  to 10 km).

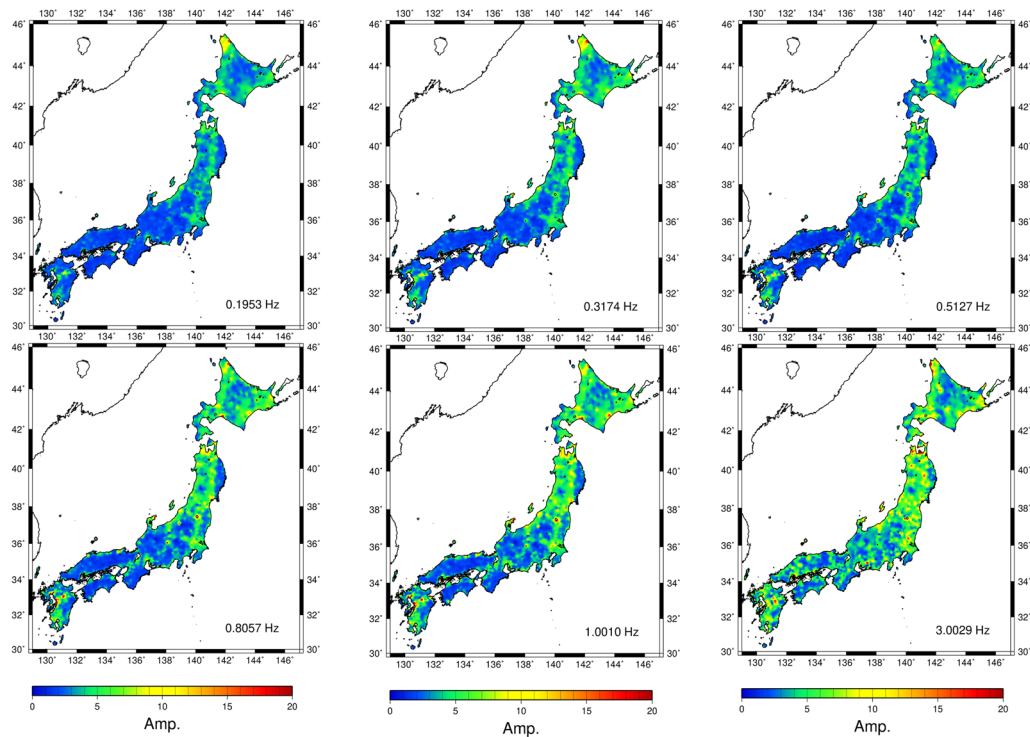
It should be noted that northeastern Japan, east of the ISTL, tends to have a higher amplitude in the SA-S than those in the southwestern Japan. This large-scale difference observed in the SA-S distribution can also be correlated to bedrock depth, as shown in Fig. 6. At 3 Hz in Fig. 5, such a correlation was not observed.



**Fig. 4** Site amplification factors with S-waves and whole-wave (SA-W) based on pseudo-velocity response spectra (pVs; with the damping  $h = 5\%$ ). Black lines represent the site amplification factors evaluated by GIT directly, using the S-wave portion of the strong-motion records. Red lines represent the site amplification calculated as shown Fig. 1, using the S-wave and coda-wave portion (i.e., whole duration after arrived S-wave) of the strong-motion records (Bold line is average; Thin line is average  $\pm 1\sigma$ )



(a) Fourier spectra



(b) pSv ( $h=5\%$ )

**Fig. 5** Spatial distribution of the site amplification with S-wave (SA-S) estimated by GIT with the S-wave portions of the strong-motion records for **a** Fourier spectra and **b** pSv

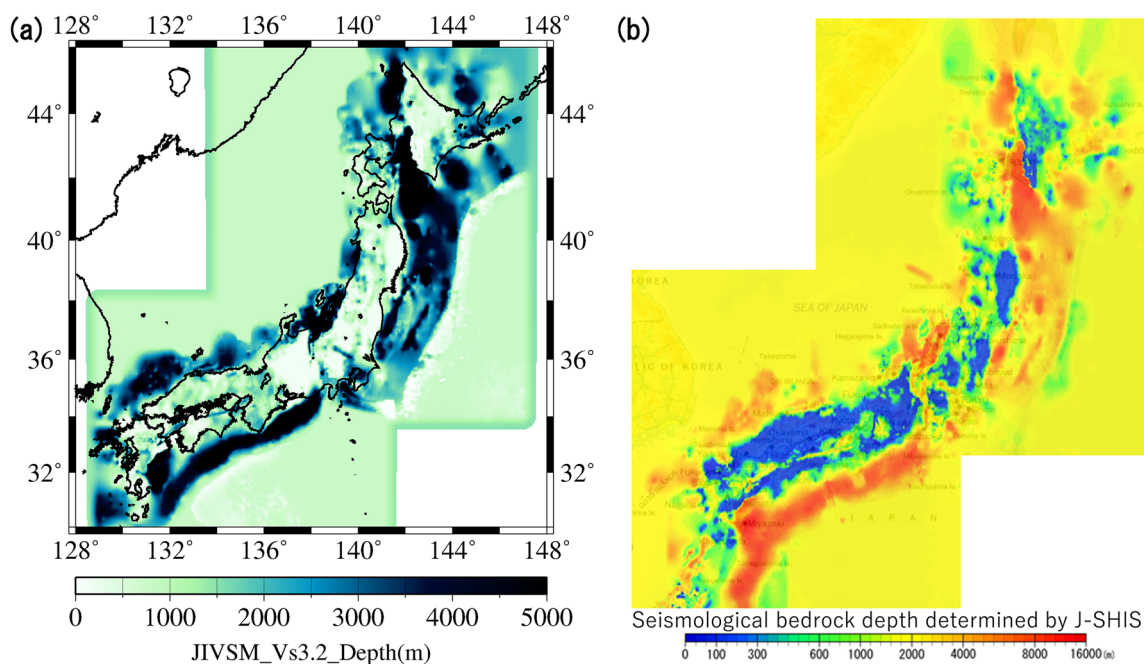


**Fig. 6** A map of the depth contour of **a** the layer with the Vs equal to 3.2 km/s from JIVSM of HERP (e.g., HERP 2012) and **b** the seismological bedrock determined by J-SHIS

Comparing the distributions of the high amplitudes in the FAS with those in the pSv, as seen in Figs. 3 and 4, indicate similarities overall. However, the amplitudes in the pSv are smoother than those in the Fourier spectra, and thus, fluctuations with frequency and space in the pSv are smaller than those in the FAS.

Figure 7 shows the spatial distribution of the SA-W using the FAS and the pSv. For comparison, we selected the figures at discrete frequencies in the same way as in Fig. 5. In Fig. 7a, the distributions of the high-amplitude areas at frequencies less than approximately 1 Hz clearly correspond to regions where the seismic bedrock depths are deeper. A typical example is the Kanto Basin (please see the red circle in the figure), where large amplitudes can be observed from as low as 0.2 Hz. Inside the large basins, the amplitudes of SA-W in Fig. 7 are much larger than those of SA-S in Fig. 5, up to 1 Hz, which is natural, as shown in Fig. 3. However, higher amplitudes can still be observed in northeastern Japan, east of the ISTL.

The amplitudes of the pSv are prominently smaller than those of the FAS. As shown in Fig. 4, the additional amplification of the SA-W in the pSv is approximately 2 at most; therefore, the amplitude and spatial distribution of the SA-W in the pSv shown in Fig. 7b are close to those of the SA-S, as shown in Fig. 5b. This is owing to the sensitivity of the FAS and the insensitivity of the pSv to the duration of motion, as already mentioned. Notably, variations in the amplitudes with respect to the frequency in

pSv are clearly smoother than those in the FAS, as seen in the SA-S. This means that the site amplification estimated from pSv might not be appropriate to capture all site-amplification characteristics at a target site; therefore, its limitations should be clearly understood prior to its use. Although it was smooth and stable, it did not fully reflect the reality of the observed ground motions.

### Differences in site amplifications by hypocentral location

As the average characteristic is useful for engineering purposes for structural designs, we focused on the average characteristic of site amplification for all events observed at each site. However, previous studies have highlighted that the predominant frequency of seismic waveforms observed at a site may change depending on the source location, that is, depth and azimuth (e.g., Terashima et al. 2015).

In this section, we discuss the variation in the predominant frequency in the SA-W by FAS depending on the source locations, relative to the average characteristics and deviations. Figure 8 shows the site amplifications evaluated from the FAS for two groups of events, classified by the predominant frequency at TKY007 in Japan. Figure 8a shows a map of the epicenters of the events where strong-motion records were observed at TKY007 located in the central Kanto Basin, indicated by a red triangle. The distributions of the sources along with their

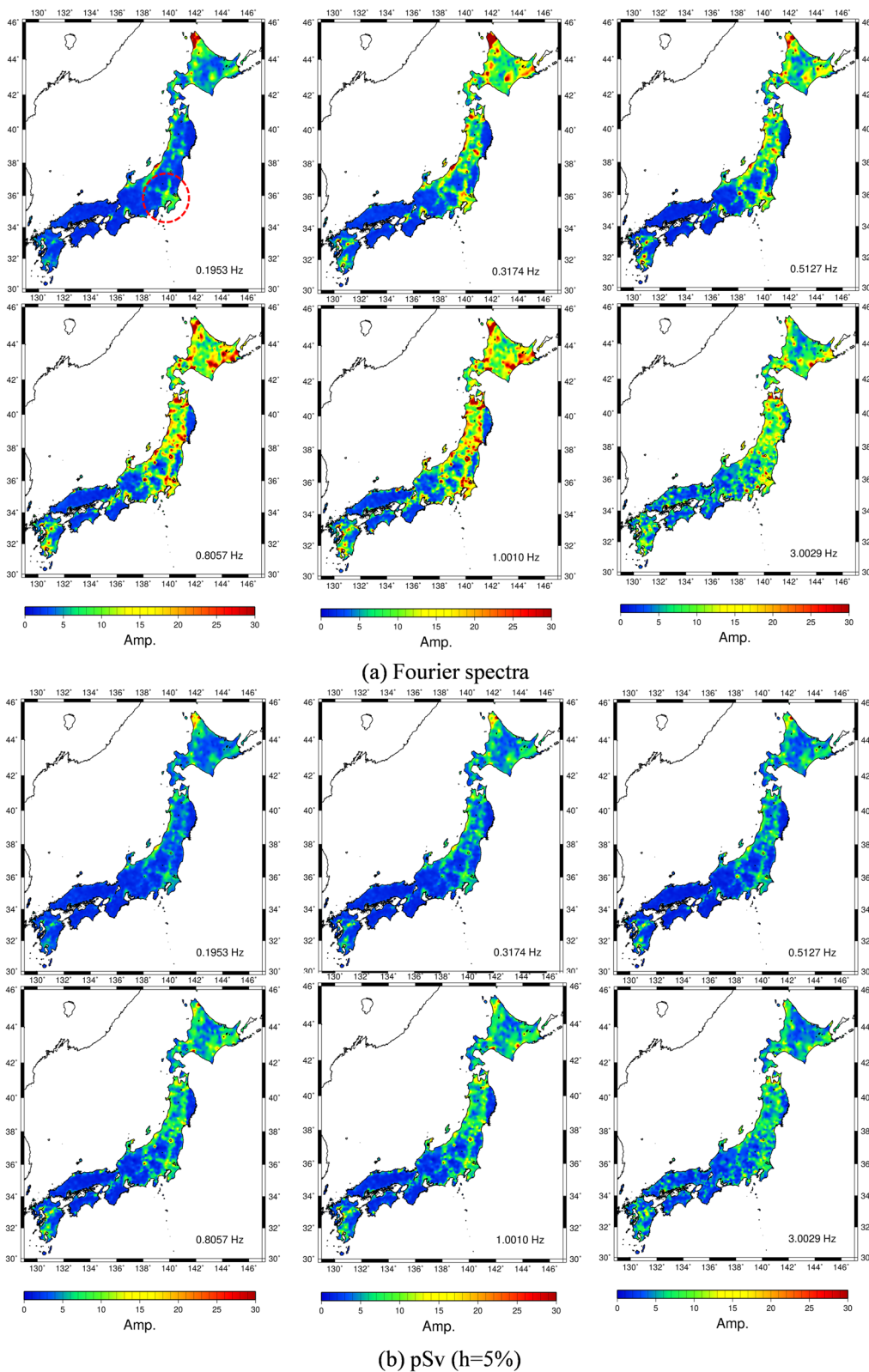


**Fig. 7** Spatial distribution of the site amplification with whole wave (SA-W) estimated using the whole duration of the strong-motion records for **a** Fourier spectra and **b** pSv

★: The events have a predominant period with around 8 s (0.125Hz) at TKY007

✕: The events do not have a predominant period with around 8 s (0.125Hz) at TKY007

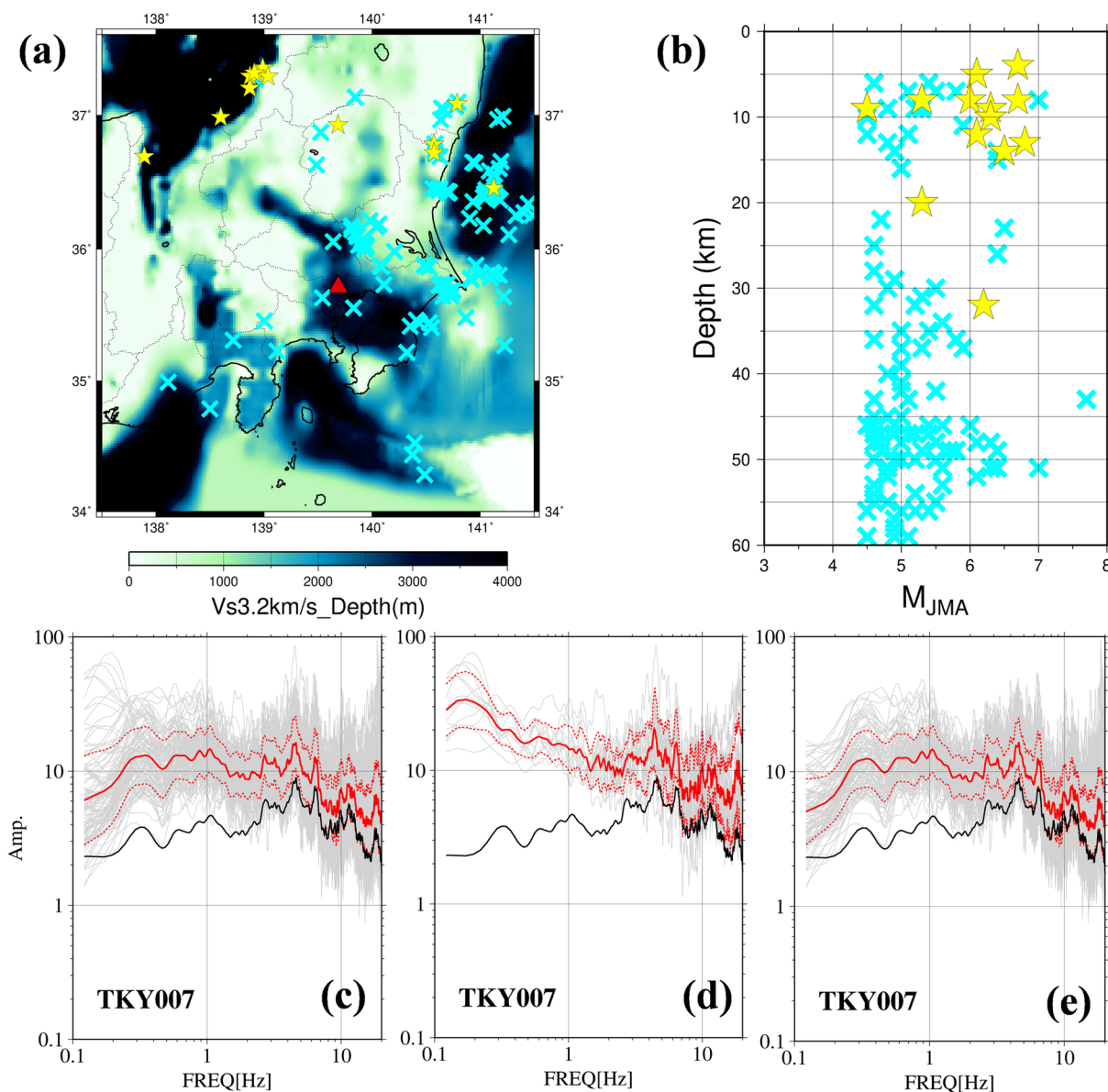


**Fig. 8** Site amplification factors with whole wave (SA-W) evaluated from Fourier spectra which were classified by the predominant frequency at TKY007 in Japan in relation to the source locations. The black line indicates SA-S, and the red line indicates SA-W. **a** Map of the epicenters of the events where strong-motion records were observed at TKY007. The star symbols represent the event with a predominant frequency around 0.125 Hz (8 s in period) in the SA-W and the cross symbols represent the other events. **b** Distributions of the source parameters with their focal depths and JMA magnitudes. **c** Site amplification terms with S-wave and whole waves calculated by all observed records used in this study at TKY007. **d** Site amplification terms with S-wave (SA-S) and whole wave (SA-W) calculated for events with a predominant frequency at 0.125 Hz at TKY007, shown by stars in **a**. **e** Site amplifications with S-wave (SA-S) and whole wave (SA-W) calculated for events without a predominant frequency at 0.125 Hz at TKY007, shown by x marks in **a**

focal depths and JMA magnitudes are shown in Fig. 8b. In these figures, the star symbols represent events with a predominant frequency of approximately 0.125 Hz (8 s in

period) in SA-W, and the x marks represent other events without such a clear low-frequency peak. In Fig. 8c–e, the black line indicates the SA-S and the red line the SA-W.

As shown in Fig. 8c, both the SA-S and SA-W were calculated from all observed records at TKY007. Figure 8d shows the SA-S and SA-W calculated from the observed records, which have a predominant frequency of 0.125 Hz (8 s in period) at TKY007. Figure 8e shows the SA-S and SA-W calculated from the observed records, which do not have such a clear predominant frequency at 0.125 Hz. As can be seen, the SA-W at TKY007 has the predominant frequency at 0.125 Hz only for events that occurred at the shallower part (predominantly less than 15 km), far from TKY007 in the north. This suggests that the predominant frequency changed considerably, depending on the source location relative to the target site. We believe that this reflects primarily the contribution of basin-induced surface waves and/or basin-transduced surface waves. Therefore, these results suggest that it is important to consider ground motion characteristics in a source- and site-specific manner.

### Correction of the site amplification at an arbitrary site

For broadband strong-motion prediction for engineering purposes at an arbitrary site considering empirical characteristics, site amplification is one of the most important factors. Based on our previous GIT studies, the SA-S estimated by the GIT is in good agreement with that from 1D ground response analysis at approximately 40% of the sites (e.g., Nakano et al. 2019; Ito et al. 2021). We need to tune the velocity models at the remaining sites for a more quantitative estimation (e.g., Nagashima et al. 2014), which will be the subject of future investigation. The SA-S is also called the horizontal site amplification factors (sHSAF) for the S-wave portion. As shown in the previous sections, we can use the SA-W or wHSAF for the whole duration as the empirical site amplification factor at the analyzed site for precise strong-motion prediction at that site. However, in many possible circumstances, observed strong-motion data are not available at the target site where a new building or facility is to be constructed.

Nakano and Kawase (2021a) recommend the following methods for estimating the SA-S without the GIT: (1) the method using observed microtremors at a target site proposed by Kawase et al. (2018) or (2) the theoretical transfer function based on the 1D theory, using a subsurface structure provided by HERP (J-SHIS or JIVSM) with PS-logging data at the target site. The SA-S can be estimated at an arbitrary site using the aforementioned methods without earthquake observations. However, the SA-S reflects only the S-wave portion and not the whole duration of motion including basin-induced surface waves and coda-waves. To account for the difference between the SA-W and SA-S, we define the WSR as a

correction function that converts the SA-S to the SA-W (e.g., Nakano 2020; Nakano and Kawase 2021a, 2021b). According to the simple expression, the WSR can be calculated using Eq. (6):

$$WSR = SA-W/SA-S, \quad (6)$$

where the SA-W is calculated by the procedure shown in Eq. (5), and the SA-S is estimated directly by the GIT. We focus on the WSR from FAS, not pSv as the latter has shown a considerable underestimation of the duration effects, as seen in Figs. 4 and 7b. This suggests the limitation of the pSv-based approach for evaluating strong ground motions over a low-frequency range. If sufficient number of observational records ( $\geq 10$ ) are available, the WSR at the observation site can be estimated by dividing the whole duration spectra by the S-wave portion spectra of the same seismic waveforms in the frequency domain. This is because the source and path characteristics are the same at the same site, and the ratio defined by Eq. (6) is equivalent to the ratio obtained by dividing the FAS of the whole duration by the FAS of the S-wave portion in the same seismic waveforms. The ratio WSR can then be easily obtained after geometrical averaging for all seismic waveforms recorded at a site. However, it should be noted that such a ratio is risky to use for a correction function from the SA-S to the SA-W because we need to evaluate SA-S from the seismological bedrock at a target site by using an independent estimation method without any guarantee for its appropriateness as SA-S, if we do not perform GIT. As we clearly defined the S-wave velocity ( $V_s$ ) at the seismological bedrock of all observation sites in our dataset as 3.45 km/s, the physical meaning of the WSR from the GIT is clear. Therefore, we believe that it is best to maintain the procedure mentioned above.

Figure 9 shows the WSR calculated using Eq. (6), based on the SA-W and SA-S directly at the same sites used in Figs. 3 and 4. The red, black, and blue lines represent the SA-W, SA-S and WSR as their ratio, respectively. As can be seen, the WSR has a smooth shape, and the amplitude varies from approximately 1 to 10. In the low-frequency range below 1 or 2 Hz, the WSR has a gentle peak with a site-dependent amplitude. In the high-frequency range over 1 or 2 Hz, the WSR becomes a monotonically decreasing function approaching 1 or 2. This smooth frequency characteristic of the WSR is a direct consequence of the spectral similarity between SA-W and SA-S.

Figure 10 shows the spatial distribution of the WSR across Japan at the six selected frequency points. The WSR is larger inside the sedimentary basins and volcanic calderas and close to 1 in mountainous areas. As was the case for the SA-S in Fig. 5, the southwestern side of Japan showed a systematically smaller WSR than the northeastern side. The spatial fluctuations of WSR are smaller than

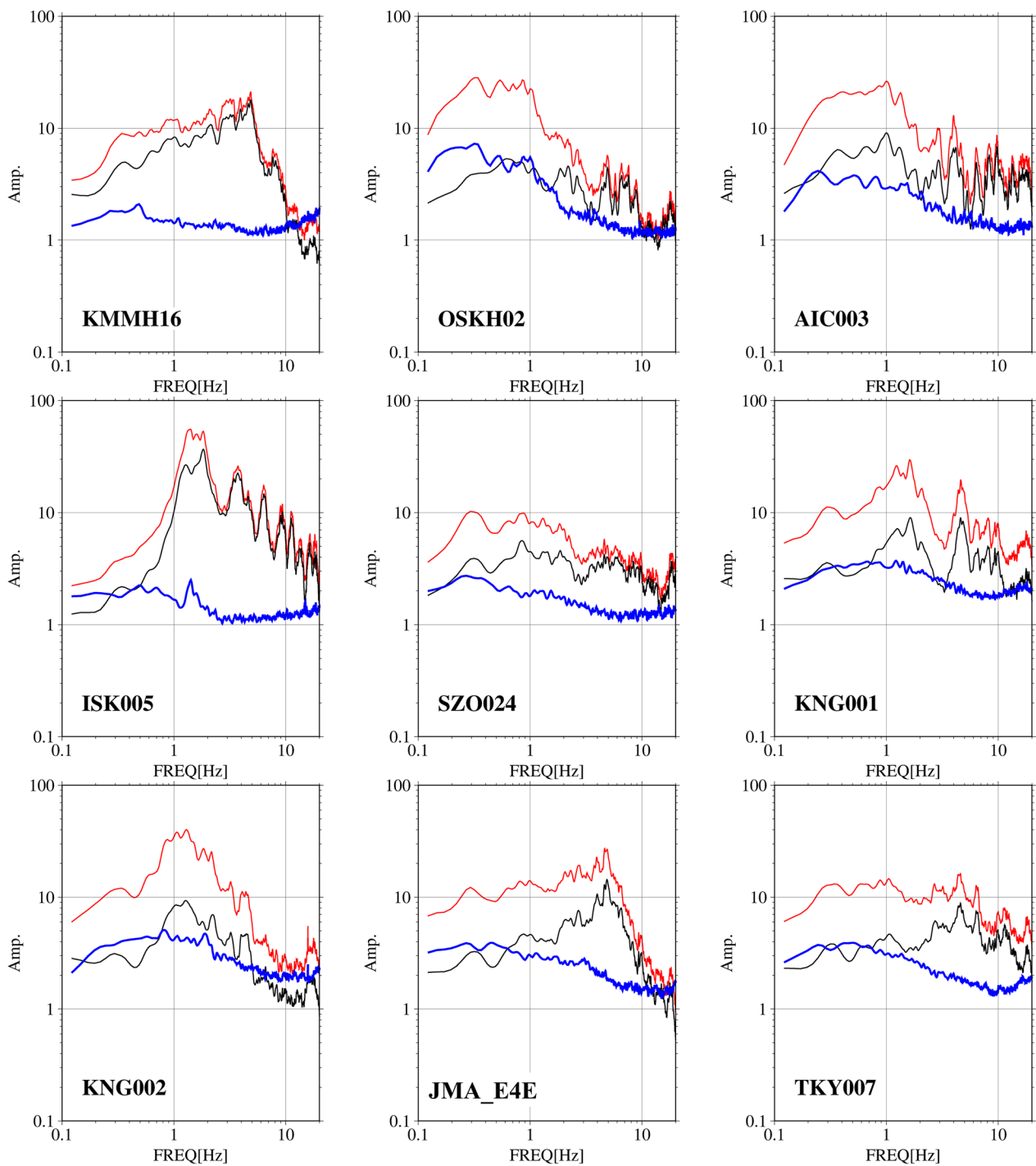


**Fig. 9** Comparison of WSR, the ratio of SA-W/SA-S, with the corresponding SA-W and SA-S spectra. Black line shows SA-S, red line shows SA-W, blue line shows WSR

those of the original site amplifications (SA-S and SA-W) shown in Figs. 5 and 7. This justifies the use of the WSR as the correction function of the SA-S for an arbitrary site to estimate the SA-W.

We adapted a two-step interpolation technique, as shown in Fig. 11. First, the WSR was estimated on the unified grid space (3 km apart) from the strong-motion observation points (Fig. 1a) using the minimum

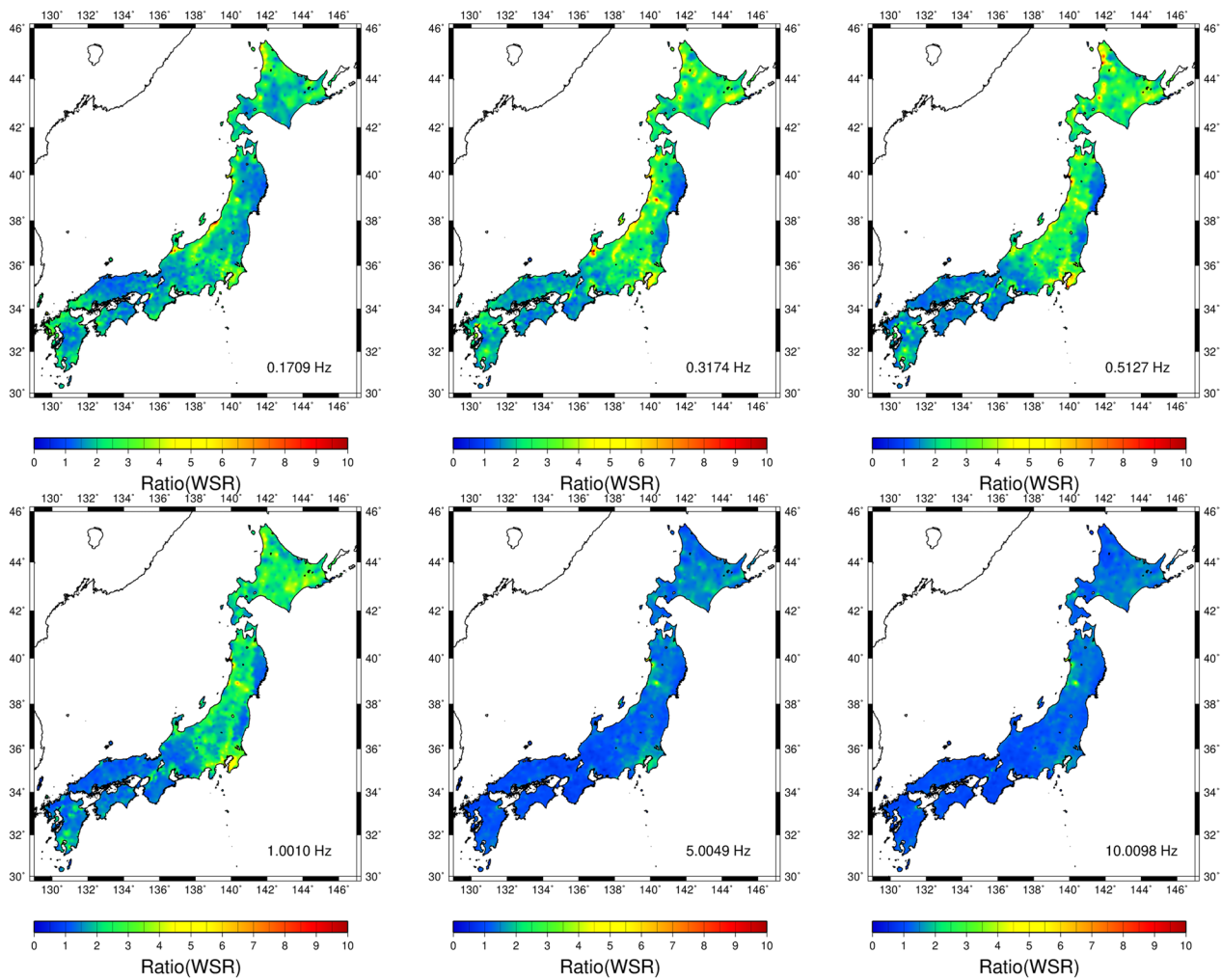


**Fig. 10** Spatial distribution of WSR at six frequency points. Color contour shows the GMT-interpolated value of WSR, where warm color represents the high value and cool color the low value

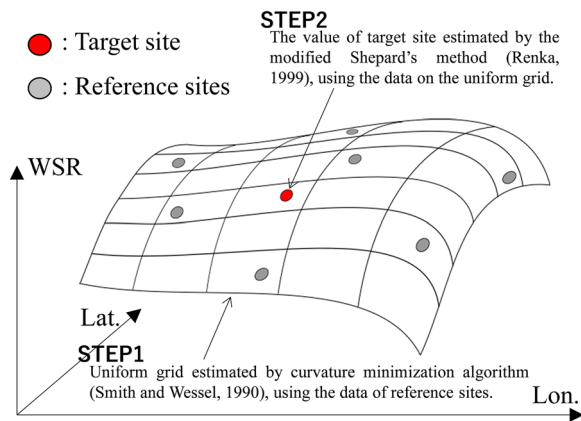


**Fig. 11** Illustration of the proposed method based on two-step spatial interpolation techniques

curvature interpolation technique proposed by Smith and Wessel (1990). Next, the WSR was evaluated at the target site employing the interpolation technique based on Shepard's method (e.g., Renka 1999), using the data interpolated on the unified grid space in the first step. These procedures were performed for all frequencies, and flowchart is shown in Fig. 12. Note that the minimum distance between the two adjacent stations ranged from 0 to 62 km, with an average of 5.8 km for all the learning sites used for interpolation, whereas and that for the test sites ranges from 0 to 24 km, with an average of 6.4 km.

Following the aforementioned procedure, the performance of the prediction scheme for the WSR was verified at an arbitrary site. First, the learning sites and the test sites in our dataset were divided as shown in Fig. 13.

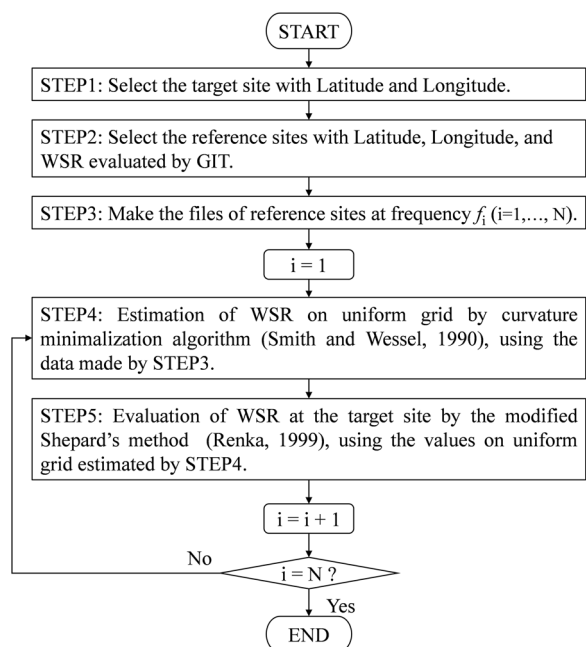


**Fig. 12** Flowchart of the proposed method in this paper based on the two-step spatial interpolation techniques

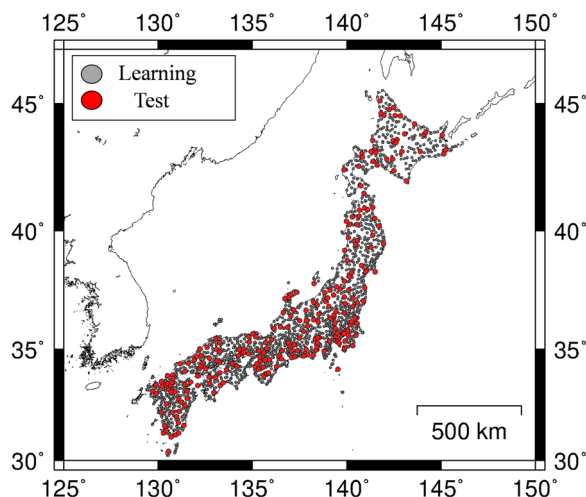


**Fig. 13** Distribution of the learning sites and the test sites used in this study. Gray closed circles show the learning sites for model construction, whereas red closed circles show the test sites for verification

In our previous studies (e.g., Nakano 2020), we used 2595 sites for GIT analysis. Prior to WSR analysis, all the WSR values at the sites were checked by visual inspection and it was found that some did not satisfy the general WSR trend, especially at a small amplitude in the high-frequency range, as mentioned above, owing to the small number of waveforms at that site. Therefore, 84 sites where waveforms of less than 2 were used to evaluate the

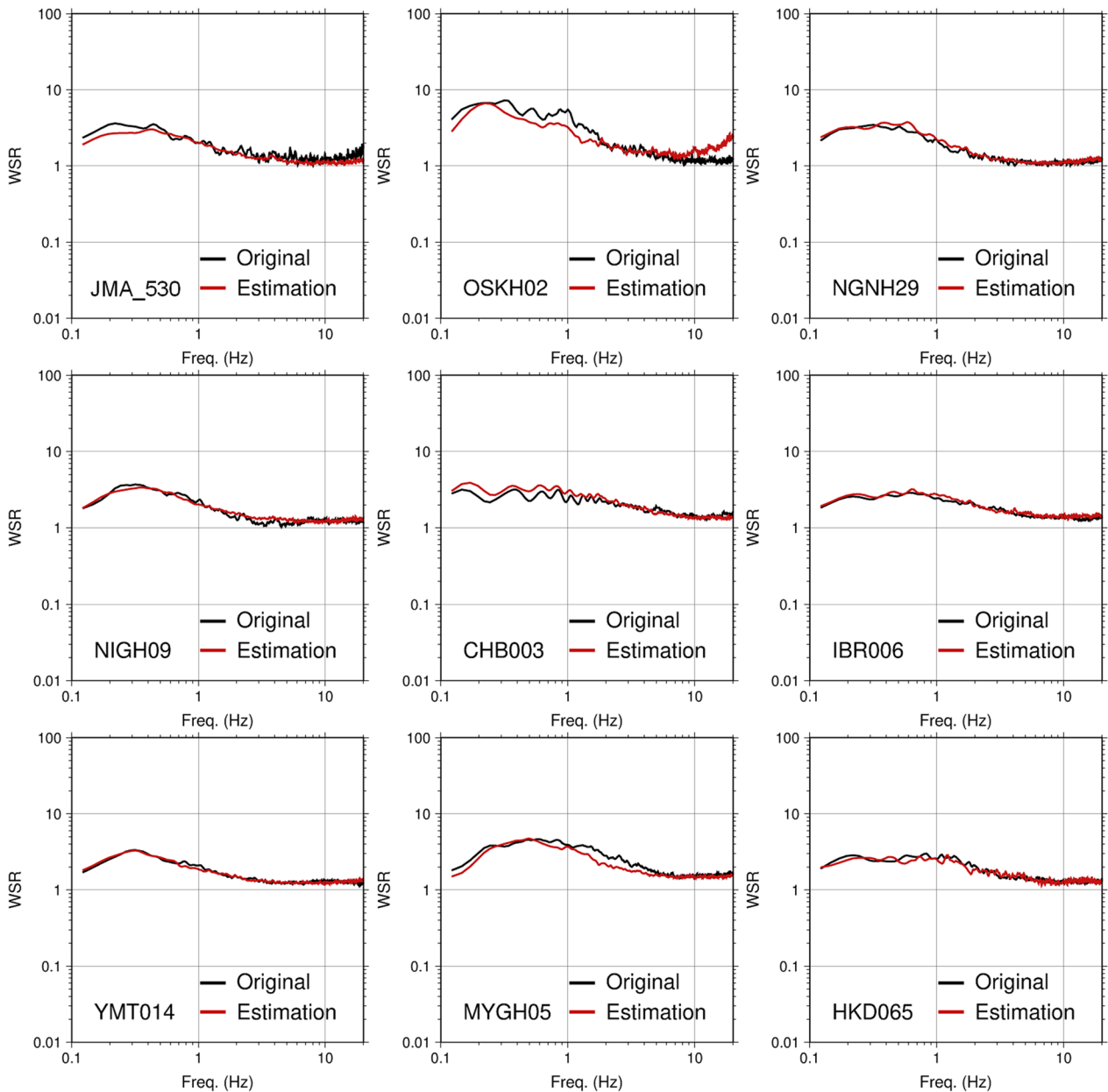
SA-S by the GIT and the 10 sites judged as inappropriate by visual inspections were excluded; and 2501 sites were selected for WSR evaluation. To verify the performance of the interpolation technique, approximately 10% of the 2501 sites (254 sites) were randomly selected as the test sites. The remaining 2247 sites were used as learning sites.

Figure 14 shows the comparison of the WSR with the original and the estimation based on the proposed method at the 9 test sites (i.e., JMA\_530, OSKH02, NGNH29, NIGH09, CHB003, IBR006, YMT014, MYGH05, and HKD065). In the figure, the black line represents the original WSR and the red line the spatially interpolated one. The amplitudes of the estimation are in good agreement with those of the original ones, and the shapes of the spectra are similar to each other, although the estimated WSR tends to be smoother.

Figure 15 shows the distribution of the WSRs (original versus estimated) for the horizontal component and the correlation coefficient ( $R^2$ ) with respect to the linear regression of the 254 test sites at the eight selected frequencies. The correlation coefficients ranged from 0.4 to 0.6.

Figure 16 shows the correlation coefficients of the WSR for both the learning and test sites at all frequency points from 0.12 to 20 Hz. The solid line shows the correlation coefficients at the test sites, whereas the dashed line shows the correlation coefficients for the learning sites. The correlation coefficients of the WSR on the learning site were high, above 0.9 in all frequencies less than approximately 10 Hz, whereas those of the WSR for the test site were above 0.5 in the frequency range between 0.25 and 3 Hz (with the maximum of 0.65 at 1.5 Hz) and above 0.4 between 0.12 and 9 Hz.

The correlation coefficients for the test sites in high frequency were considerably lower than those of the learning sites, primarily because the range of the WSR decreases as the target frequency increases, and therefore, a small number of outliers can easily break the proportionality between observation and interpolation (Fig. 16). However, considering the similarity of the shapes of the WSRs, as shown in Fig. 15, as well as those shown in the Additional files 1, 2, 3, 4, 5, 6, 7, 8, 9, 10 and 11 where we provide the observed and estimated WSRs at all 254 sites, the capability of the proposed estimation method based on the WSR would be sufficient for SA-W evaluation, in which we need only the location information (i.e., latitude and longitude) of an arbitrary site, provided that we have an estimated SA-S calculated by either microtremors (e.g., Kawase et al. 2018) or the theoretical transfer function of S-waves (e.g., Senna et al. 2013; Ito et al. 2021).



**Fig. 14** Comparison of the WSRs predicted by the proposed method in this study at the test sites with the original WSRs. The black line represents the original WSR and the red line the estimated one

**Discussion**

In this section, we discuss the correlation of WSRs with the number of waveforms and the average distance between the target site and the three sites nearest to the target site among the learning sites that we selected in the previous section by checking the residuals with respect to the original data. We believe that this discussion will lead to the identification of significant factors for predicting site amplifications using an empirical approach.

To evaluate the performance of the WSRs, we calculated the residuals defined by Eq. (7):

$$\varepsilon_j = \frac{(\text{Cal}_j - \text{Obs}_j)^2}{((\text{Cal}_j)^2 \cdot (\text{Obs}_j)^2)^{0.5}}, \tag{7}$$

where  $\varepsilon_j$  is the residual of the estimation value and original data at the  $j$ th target site, “Cal”, which stands for calculated, represents the estimation value of the WSR at a

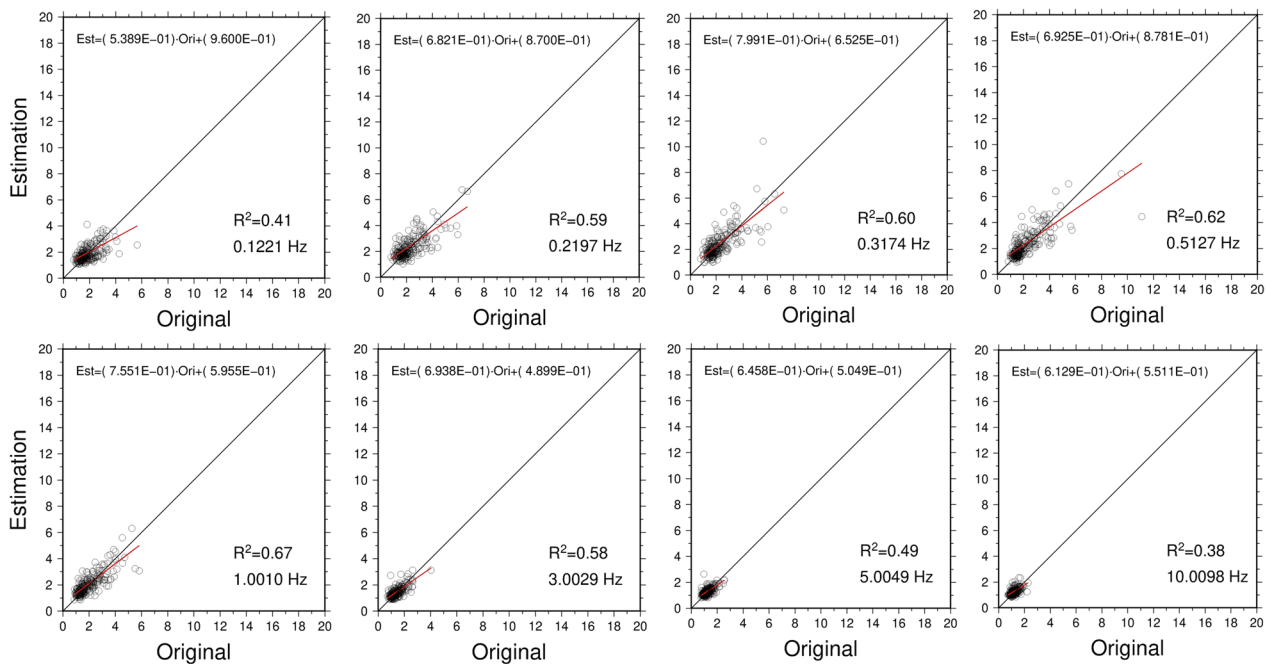


**Fig. 15** Distribution of WSRs (observed versus estimated) and their correlation coefficients on the test sites at several selected frequencies

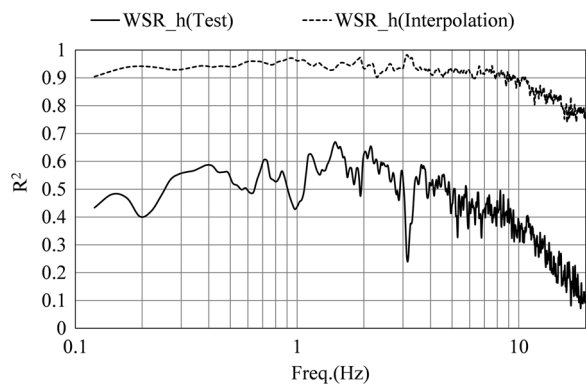


**Fig. 16** Correlation coefficient of WSRs for the learning sites (directly interpolation with learning data) and the test sites at all frequency points

target site by the proposed method in the previous section, and “Obs”, which stands for observation, represents the original value of the WSR at the same target site. We used the logarithmic value to calculate the residuals.

The target of WSRs is to correct the SA-S, especially in the low-frequency range. Thereby, we set the bins at the six frequency ranges as 0.0–0.5 Hz, 0.5–1.0 Hz, 1.0–1.5 Hz, 1.5–2.0 Hz, 2.0–2.5 Hz, and 2.5–3.0 Hz.

The number of waveforms used for the estimation is an important factor for evaluating site amplification in the empirical approach. Perron et al. (2022) suggested

that the minimum required number of waveforms for estimating site amplification is approximately 10. They also suggested that the higher the number of waveforms, the lower the uncertainty of site amplification. Therefore, it can be expected that the higher the number of waveforms, the lower the residuals obtained using the estimation of the WSRs. Furthermore, we adapted the interpolation technique to predict the WSR at an arbitrary site (which has the same meaning as “a target site”) and therefore assume that the distance from the sites of learning data for interpolation to the target site is also important.

From the above, two indices were selected to confirm the properties of the residuals as the number of waveforms obtained at the target site among the test sites that we selected in the previous section and the distance between the target site and the nearest three sites among the learning sites selected in the previous section. To compare the number of waveforms, 14 categories of the number of waveforms were set to 0–10, 10–20, 20–30, 30–40, 40–50, 50–60, 60–70, 70–80, 80–100, 100–150, 150–200, 200–300, 300–400, and >400. Here, the number of waveforms was counted at the test sites selected in the previous section. Further, six distance categories: 0–3 km, 3–5 km, 5–10 km, 10–15 km, 15–20 km, and over 20 km, were set for comparison by the average distance between the target site and the nearest three sites among the learning sites selected in the previous section.

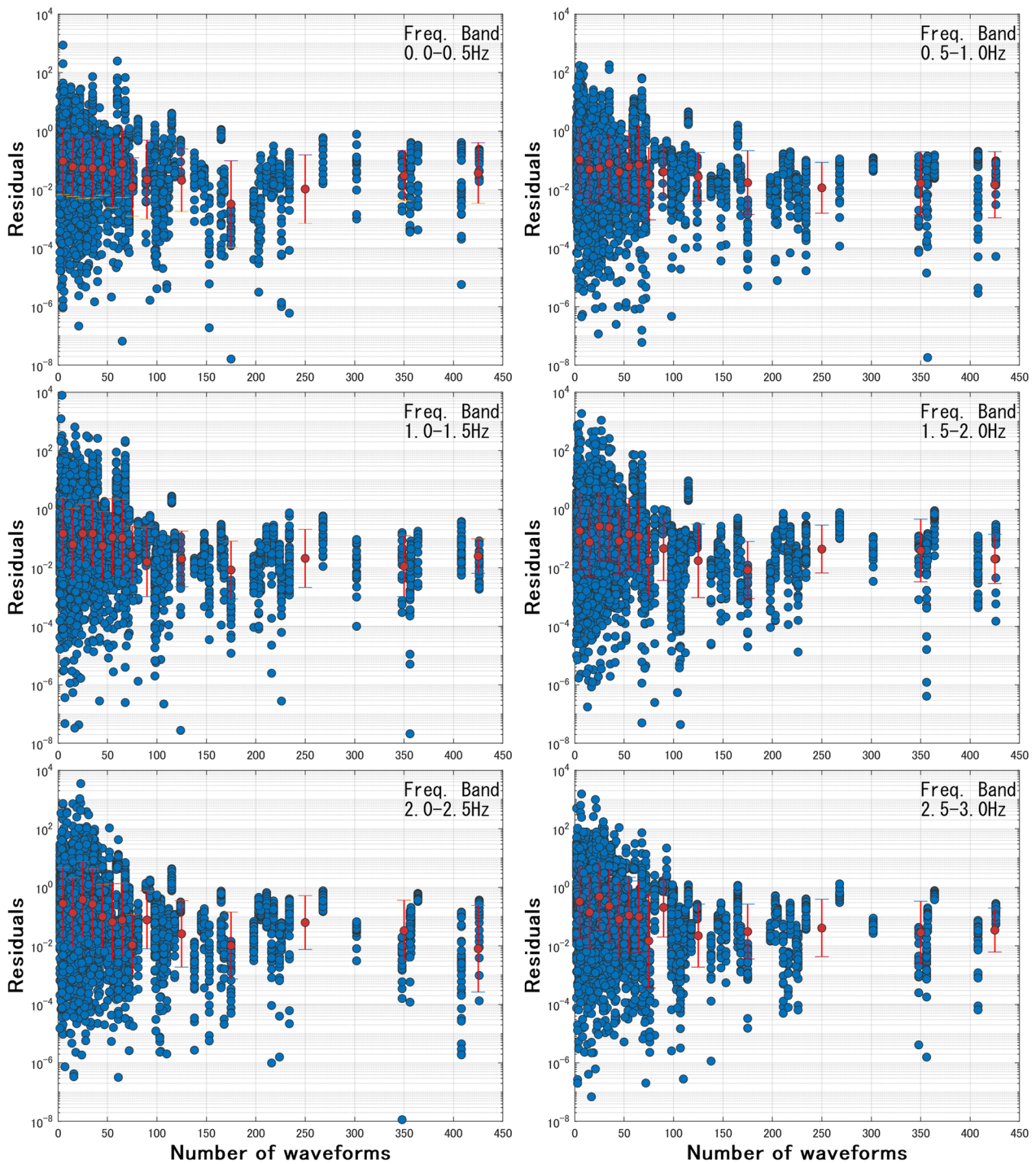


**Fig. 17** Comparison of the residuals of WSR calculated by the proposed method with the number of waveforms

Figure 17 shows a comparison of the residuals of the WSR calculated using Eq. (7) with the number of waveforms. These values were plotted for each frequency category. The number of circles on Fig. 17 (and Fig. 18 showed later) is larger than the 254 target sites, because

we showed all the residuals, which are different at each frequency, in each frequency category. The logarithmic average values and the range of standard deviations by the 14 categories of the number of waveforms were plotted in the same figure. While the deviations of the

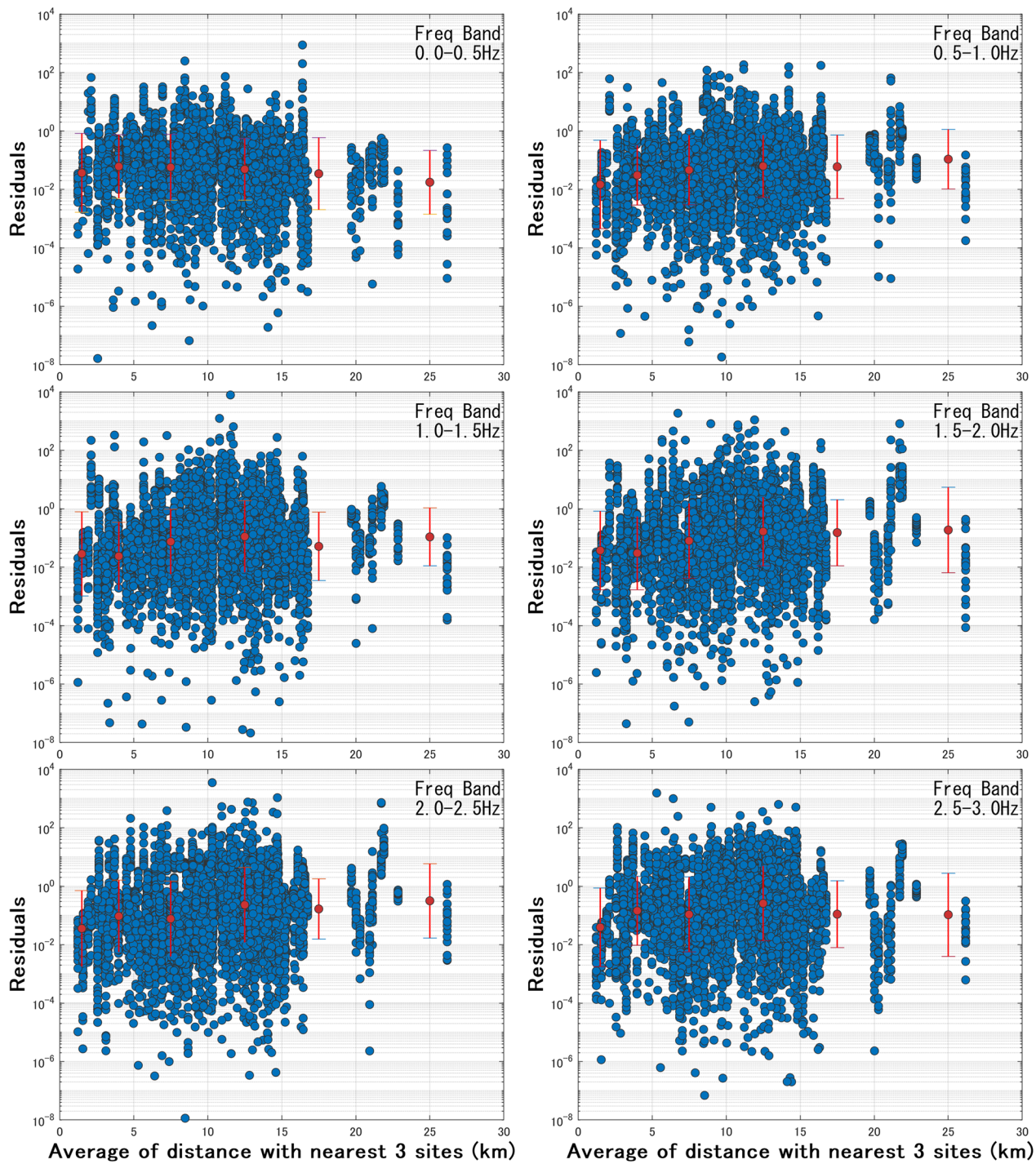


**Fig. 18** Comparison of the residuals of WSR calculated by the proposed method with the average distance between the target site and the nearest three sites among the learning sites

residuals by the number of waveforms were large, the residuals were slightly decreased by increasing the number of waveforms. This trend can be understood based on the studies mentioned above.

Figure 18 shows a comparison of the residuals of the WSR calculated by Eq. (7), with the average distance between the target site and the nearest three sites among the learning sites selected in the previous section. These

values were plotted for each frequency category. We plotted the logarithmic average values and the range of standard deviations for the 6 categories with the range of average distance in the same figure. While the deviations of the residuals by the average distance were as large as those in Fig. 17, the residuals were slightly increased by increasing the average distance, excluding the range of 0–0.5 Hz. In the panels higher than 0.5 Hz, this is expected, according to the studies mentioned above. However, it is still unclear why, against a physical background, the residuals in the range of 0–0.5 Hz did not clearly depend on the waveform number. We will further investigate this in our future studies.

### Conclusion

We used the generalized inversion technique (GIT) to estimate the empirical characteristics applying FAS and pSv for all sites of K-NET, KiK-net, the JMA network of 87 and 95 types, and the CEORKA network in the Kansai area. The SA-S and SA-W were evaluated in a two-step procedure. We investigated the average characteristics of the site amplifications, not only with the amplitude in the frequency domain at each site, but also with the spatial distributions. After investigating the fundamental characteristics of the SA-W relative to the SA-S for FAS, we proposed the use of the ratio between them as the WSR and its two-step interpolation scheme in space for prediction.

The results obtained in the present study can be summarized as follows:

- The distributions of the high-amplitude area at frequencies less than approximately 1 Hz clearly correspond to the region where the seismic bedrock is deeper than the other areas geologically. Because of good correlation of SA-S with the depth to the seismic bedrock, the variation in space for SA-S in the frequency range lower than 1 Hz is small enough to make it possible to interpolate SA-S from several nearby sites.
- The site amplifications obtained with the whole wave, SA-W, are larger than those obtained with the S-wave, SA-S, in the frequency range less than 1–2 Hz, while both are similar in a higher frequency range. The spatial distributions of the SA-W clearly reflected the spatial variation of the geological structure in a low-frequency range. In particular, the high-amplitude areas corresponded remarkably well to the regions where the seismic bedrock depths were deeper, as in the case of the SA-S. This suggests that we can easily predict site amplifications using an empirical approach through spatial interpolation, based on the empirical properties obtained here.
- The amplitudes of the site amplifications separated from the pSv are significantly smaller than those from the FAS, regardless of the SA-S or SA-W, except for the frequency range below the fundamental peak frequency. The amplitude fluctuations with frequency in both the SA-S and SA-W from the pSv were clearly smoother than those from the FAS. This can be explained by the difference in the physical background of the FAS and the pSv. This suggests that the site amplifications estimated via pSv might not reflect the physical frequency characteristics at a target site; therefore, the pSv needs to be used with caution, especially for its insensitivity to the duration of motion, as clearly seen in the SA-W.
- The general shapes of the spatial distributions of the SA-S evaluated by FAS and pSv are similar to each other in the lower frequency range, below approximately 1 Hz, although their amplitudes are different from each other.
- To investigate the effect of source locations on the SA-W, we selected one site inside a large basin and see fluctuation of SA-W with respect to the source azimuths and depths. We found that the predominant frequency changes significantly depending on the source location. Thereby, it is important to consider where an earthquake will occur relative to a target site in future strong-motion predictions for more quantitative prediction on the SA-W.
- The WSR was stable in the shape of the spectra, and the WSR fluctuations with the spatial distributions in Fig. 10 are apparently smaller than those of the original SA-S or SA-W, as shown in Figs. 5 and 7. This means that we can use the WSR as the correction function for the SA-S for an arbitrary site. We also found that the spatial distributions of the site amplifications for the S-wave portion (SA-S) were relatively similar in a close area for a long-period range from 2 to 8 s, especially inside large sedimental basins (e.g., the Kanto or Osaka Basin). It suggests that we could easily predict the site amplifications with the empirical approach through a spatial interpolation based on the properties at nearby sites obtained by GIT.
- We propose a simple correction scheme for converting the SA-S to the SA-W, based on the spatial interpolation of the WSR. The correlation coefficients for WSRs at the test sites, not used as control points in the interpolation, with respect to the observed WSR were not so high (0.4–0.65); however, because of the similarity of the WSR spectral shapes seen in Fig. 14 and figures in the Additional files 1–11, the capability of the proposed correction scheme based on WSRs for the quantitative estimation of the SA-W is verified as long as we can estimate SA-S independently.

- We checked the residuals of the estimation values of the WSR using the proposed method at the test sites with respect to the original data. The residuals were slightly dependent on the number of waveforms at the test site as well as the average distance between the test sites and the nearest three sites among the learning sites selected in the previous section.

In this study, we report the empirical correction method based on the average characteristics of the WSR all over Japan, derived from two-step GIT analyses using observed strong-motion records. We plan to investigate the physical mechanisms of the generation of the observed WSR spectra for better prediction, with a quantitative representation of the source location dependency, as shown in Fig. 8. We also report the characteristics of vertical site amplifications in Japan in a separate article.

#### Abbreviations

CEORKA	Committee of Earthquake Observation and Research in the Kansai Area
GIT	Generalized inversion technique
GMM	Ground motion model
GMPE	Ground motion prediction equation
HERP	Headquarters for Earthquake Research Promotion in Japan
HSAF	Horizontal site amplification factor
ISTL	Itoigawa–Shizuoka Tectonic Line
JIVSM	Japan Integrated Velocity Structure Model
JMA	Japan Meteorological Agency
JMBSC	Japan Meteorological Business Support Center
J-SHIS	Japan Seismic Hazard Information Station
NIED	National Research Institute for Earth Science and Disaster Resilience in Japan
SDOF	Single degree of freedom system
WSR	Whole-duration and S-wave portion spectral Ratio

#### Supplementary Information

The online version contains supplementary material available at <https://doi.org/10.1186/s40623-023-01800-z>.

**Additional file 1. Comparison of WSRs between original and estimation [1/11].**

**Additional file 2. Comparison of WSRs between original and estimation [2/11].**

**Additional file 3. Comparison of WSRs between original and estimation [3/11].**

**Additional file 4. Comparison of WSRs between original and estimation [4/11].**

**Additional file 5. Comparison of WSRs between original and estimation [5/11].**

**Additional file 6. Comparison of WSRs between original and estimation [6/11].**

**Additional file 7. Comparison of WSRs between original and estimation [7/11].**

**Additional file 8. Comparison of WSRs between original and estimation [8/11].**

**Additional file 9. Comparison of WSRs between original and estimation [9/11].**

**Additional file 10. Comparison of WSRs between original and estimation [10/11].**

**Additional file 11. Comparison of WSRs between original and estimation [11/11].**

#### Acknowledgements

We used waveforms published by the JMA, CEORKA, K-NET, and KiK-net. We illustrated a few graphs using GMT (Wessel and Smith 1998) and/or ViewWave (Kashima 2021). We appreciate all the persons concerned with these projects.

#### Author contributions

KN performed most of the analyses using the GIT, following the advice from HK. KN wrote the initial draft of the manuscript through discussions with HK. The final manuscript was written by both authors, based on the discussion in this manuscript. All authors read and approved the final manuscript.

#### Funding

None.

#### Availability of data and materials

The waveforms used in this study are available from CEORKA, K-NET, KiK-net, and JMA. The waveforms of the JMA were published by the JMBSC (<http://www.jmbc.or.jp/jp/>; accessed 2022.09.20). The waveforms of CEORKA were published by the authors themselves (<http://www.ceorka.org/>; accessed at 2022.09.20).

#### Declarations

#### Competing interests

The authors declare that they have no competing interests.

#### Author details

<sup>1</sup>Technical Research Institute, HAZAMA ANDO CORPORATION, 515-1 Karima, Tsukuba 305-0822, Japan. <sup>2</sup>Disaster Prevention Research Institute, Kyoto University, Gokasho, Uji, Kyoto 611-0011, Japan.

Received: 30 September 2022 Accepted: 5 March 2023

Published online: 04 May 2023

#### References

- Abrahamson N, Atkinson G, Boore D, Bozorgnia Y, Campbell K, Chiou B, Idriss I, Silva W, Youngs R (2008) Comparison of the NGA ground-motion relations. *Earthq Spectra* 24(1):45–66. <https://doi.org/10.1193/1.292436>
- Abrahamson NA, Kuehn NM, Walling M, Landwehr N (2019) Probabilistic seismic hazard analysis in California using nonergodic ground-motion models. *Bull Seismol Soc Am* 109(4):1235–1249. <https://doi.org/10.1785/0120190030>
- Andrews DJ (1982) Separation of source and propagation spectra of seven Mammoth Lakes aftershocks. In: Proceedings of workshop 16, dynamic characteristics of fault, U S Geol Sur Open File Rep, pp 82–591
- Bard PY, Bouchon M (1980b) The seismic response of sediment-filled valleys. Part 2. The case of incident P and SV waves. *Bull Seismol Soc Am* 70(5):1921–1941. <https://doi.org/10.1785/BSSA0700051921>
- Bard PY, Bouchon M (1980a) The seismic response of sediment-filled valleys. Part 1. The case of incident SH waves. *Bull Seismol Soc Am* 70(4):1263–1286. <https://doi.org/10.1785/BSSA0700041263>
- Bindi D, Spallarossa D, Pacor F (2017) Between-event and between-station variability observed in the Fourier and response spectra domains: comparison with seismological models. *Geophys J Int* 210:1092–1104. <https://doi.org/10.1093/gji/ggx217>
- Bora S, Scherbaum F, Kuehn N, Stafford P (2016) On the relationship between Fourier and response spectra: implications for the adjustment of empirical ground-motion prediction equations (GMPEs). *Bull Seismol Soc Am* 106(3):1235–1253. <https://doi.org/10.1785/0120150129>

- Bozorgnia Y, Abrahamson NA, Al Atik L, Ancheta TD, Atkinson GM, Baker JW, Baltay A, Boore DM, Campbell KW, Chiou BS-J, Darragh R, Day S, Donahue J, Graves RW, Gregor N, Hanks T, Idriss IM, Kamai R, Kishida T, Kottke A, Mahin SA, Rezaeian S, Rowshandel B, Seyhan E, Shahi S, Shantz T, Silva W, Spudich P, Stewart JP, Watson-Lamprey J, Wooddell K, Youngs R (2014) NGA-West2 research project. *Earthq Spectra* 30(3):973–987. <https://doi.org/10.1193/072113EQS209M>
- Dhakal YP, Sasatani T, Takai N (2011) Validation of the deep velocity structure of the Tokachi basin based on 3-D simulation of long-period ground motions. *Pure Appl Geophys* 168:1599–1620. <https://doi.org/10.1007/s00024-010-0237-3>
- Fukushima Y, Tanaka T (1990) A new attenuation relation for peak horizontal acceleration of strong earthquake ground motion in Japan. *Bull Seismol Soc Am* 80(4):757–783. <https://doi.org/10.1785/BSSA0800040757>
- Furumura T (2014) Risk of long-period ground motion due to the deep basement structure of the Kanto Basin. *J Geogr (chigaku Zasshi)* 123(4):434–450. <https://doi.org/10.5026/jgeography.123.434>
- Headquarters for Earthquake Research Promotion (2012) Long-period ground motion prediction map. [https://www.jishin.go.jp/evaluation/seismic\\_hazard\\_map/lpshm/12\\_choshuki/](https://www.jishin.go.jp/evaluation/seismic_hazard_map/lpshm/12_choshuki/). Accessed at 10 Dec 2022
- Hudson DE (1962) Some problems in the application of spectrum techniques to strong-motion earthquake analysis. *Bull Seismol Soc Am* 52(2):417–430. <https://doi.org/10.1785/BSSA0520020417>
- Ito E, Nakano K, Senna S, Kawase H (2021) S-wave site amplification factors from observed ground motions in Japan: validation of delineated velocity structures and proposal for empirical correction. *Earthquakes*. <https://doi.org/10.5772/intechopen.95478>
- Joyner WB, Boore DM (1981) Peak horizontal acceleration and velocity from strong-motion records including records from the 1979 Imperial Valley, California, earthquake. *Bull Seismol Soc Am* 71(6):2011–2038. <https://doi.org/10.1785/BSSA0710062011>
- Joyner WB, Boore DM (1993) Methods for regression analysis of strong-motion data. *Bull Seismol Soc Am* 83(2):469–487. <https://doi.org/10.1785/BSSA0830020469>
- J-SHIS (2020) <https://www.j-shis.bosai.go.jp/map/?lang=en>. Accessed at 16 Dec 2022
- Kashima T (2021) ViewWave. <https://smo.kenken.go.jp/~kashima/viewwave>. Accessed at 10 Dec 2022
- Kataoka S, Satoh T, Matsumoto S, Kusakabe T (2006) Attenuation relationships of ground motion intensity using short period level as a variable. *J Jpn Soc Civil Eng* 62(4):740–757. <https://doi.org/10.2208/jsej.62.740>. **(in Japanese with English abstract)**
- Kawase H (1993) Review: amplification of seismic waves by sedimentary layers and its simulation. *Zisin Ser II* 46(2):171–190. [https://doi.org/10.4294/zisin1948.46.2\\_171](https://doi.org/10.4294/zisin1948.46.2_171). **(in Japanese with English abstract)**
- Kawase H (2006) Site effects derived from spectral inversion method for K-NET, KiK-net, and JMA strongmotion network with special reference to soil nonlinearity in high PGA records. *Bull Earthq Res Inst Tokyo Univ* 81:309–315
- Kawase H (2021) History of our understanding on the effects of surface geology on seismic motions: Can we see a new horizon? In: The 6th IASPEI/IAEE international symposium: the effects of surface geology on seismic motion, ESG-K01
- Kawase H, Aki K (1989) A study on the response of a soft basin for incident S, P, and Rayleigh waves with special reference to the long duration observed in Mexico City. *Bull Seismol Soc Am* 79(5):1361–1382. <https://doi.org/10.1785/BSSA0790051361>
- Kawase H, Matsuo H (2004) Separation of source, path, and site effects based on the observed data by K-NET, KiK-net, and JMA strong motion network. *J Jpn Assoc Earthq Eng* 4(1):33–52. <https://doi.org/10.5610/jaee.4.33>. **(in Japanese with English abstract)**
- Kawase H, Nagashima F, Nakano K, Mori Y (2018) Direct evaluation of S-wave amplification factors from microtremor H/V ratios: double empirical corrections to “Nakamura” method. *Soil Dyn Earthq Eng*. <https://doi.org/10.1016/j.soildyn.2018.01.049>
- Kodera Y, Yamada Y, Hirano K, Tamaribuchi K, Adachi S, Hayashimoto N, Morimoto M, Nakamura M, Hoshiba M (2018) The Propagation of Local Undamped Motion (PLUM) method: a simple and robust seismic wave-field estimation approach for earthquake early warning. *Bull Seismol Soc Am* 108(2):983–1003. <https://doi.org/10.1785/0120170085>
- Montejo LA, Vidot-Vega AL (2017) An empirical relationship between Fourier and response spectra using spectrum-compatible times series. *Earthq Spectra* 33(1):179–199. <https://doi.org/10.1193/060316eqs089m>
- Nagashima F, Matsushima S, Kawase S, Sánchez-Sesma FJ, Hayakawa T, Satoh T, Oshima M (2014) Application of horizontal-to-vertical spectral ratios of earthquake ground motions to identify subsurface structures at and around the K-NET site in Tohoku, Japan. *Bull Seismol Soc Am* 104(5):2288–2302. <https://doi.org/10.1785/0120130219>
- Nakano K, Kawase H (2019) Source parameters and site amplifications estimated by generalized inversion technique: focusing on the 2018 Hokkaido Iburi-Tobu earthquake. *Earth Planets Space* 71:66. <https://doi.org/10.1186/s40623-019-1047-1>
- Nakano K, Kawase H (2021a) A study on the strong motion prediction method based on the characteristics estimated by generalized inversion technique. *J Jpn Assoc Earthq Eng* 21(2):130–153. [https://doi.org/10.5610/jaee.21.2\\_130](https://doi.org/10.5610/jaee.21.2_130). **(in Japanese with English abstract)**
- Nakano K, Kawase H (2021b) Spatial properties of the site amplifications evaluated by generalized inversion technique with Fourier spectra and response spectra. In: The 6th IASPEI/IAEE international symposium: the effects of surface geology on seismic motion, GS5-P03
- Nakano K, Kawase H, Matsushima S (2015) Statistical properties of strong ground motions from the generalized spectral inversion of data observed by K-NET, KiK-net, and the JMA shindokei network in Japan. *Bull Seismol Soc Am* 105(5):2662–2680. <https://doi.org/10.1785/0120140349>
- Nakano K, Kawase H, Matsushima S (2019) A study on the site amplifications estimated by generalized inversion technique. *J Jpn Assoc Earthq Eng* 19(2):1–24. [https://doi.org/10.5610/jaee.19.2\\_1](https://doi.org/10.5610/jaee.19.2_1). **(in Japanese with English abstract)**
- Nakano K (2020) A strong-motion prediction method based on the characteristics estimated by generalized inversion technique. PhD dissertation, Graduate School of Kyoto University. <https://doi.org/10.14989/doctor.k22407>. **(in Japanese)**
- National Research Institute for Earth Science and Disaster Resilience (2019) NIED K-NET, KiK-net. National Research Institute for Earth Science and Disaster Resilience. <https://doi.org/10.17598/NIED.0004>
- Perron V, Paolo B, Donat F (2022) Evaluating the minimum number of earthquakes in empirical site response assessment: input for new requirements for microzonation in the Swiss building codes. *Front Earth Sci* 10:91855. <https://doi.org/10.3389/feart.2022.917855>
- Renka R (1999) Algorithm 790: CSHEP2D: cubic Shepard method for bivariate interpolation of scattered data. *ACM Trans Math Softw* 25(1):70–73. <https://doi.org/10.1145/305658.305737>
- Satoh T, Sato T, Kawase H, Uetake T (1998) Difference of regression coefficients for response and Fourier spectra of strong-motion records and its interpretation. *J Struct Const Eng (trans AIJ)* 63(506):83–92. [https://doi.org/10.3130/aijs.63.83\\_1](https://doi.org/10.3130/aijs.63.83_1)
- Satoh T, Okawa I, Nishikawa T, Sato T, Seki M (2010) Prediction of waveforms of long-period ground motions for hypothetical earthquakes using empirical regression relations of response spectra and phase spectra. *J Struct Const Eng (trans AIJ)* 75(649):521–530. <https://doi.org/10.3130/aijs.75.521>. **(in Japanese with English abstract)**
- Senna S, Maeda T, Inagaki Y, Suzuki H, Matsuyama H, Fujiwara H (2013) Modeling of the subsurface structure from the seismic bedrock to the ground surface for a broadband strong motion evaluation. *J Disaster Res* 8(5):889–903. <https://doi.org/10.20965/jdr.2013.p0889>
- Smith FHW, Wessel P (1990) Gridding with continuous curvature splines in tension. *Geophysics* 55:3. <https://doi.org/10.1190/1.1442837>
- Terashima Y, Hirai T, Fukuwa N (2015) The effect of sedimentary basin structure on predominant period of seismic ground motion. *J Struct Const Eng (trans AIJ)* 80(708):219–229. <https://doi.org/10.3130/aijs.80.219>. **(in Japanese with English abstract)**
- Ueno H, Hatakeyama S, Aketagawa T, Funasaki J, Hamada N (2002) Improvement of hypocenter determination procedures in the Japan Meteorological Agency. *Q J Seismol* 65:123–134. **(in Japanese)**
- Wakai A, Senna S, Jin K, Yatagai A, Suzuki H, Inagaki W, Matsuyama H, Fujiwara H (2019) Modeling of subsurface velocity structures from seismic bedrock to ground surface in the Tokai region, Japan, for broadband strong ground motion prediction. *J Disaster Res* 14(9):1140–1153. <https://doi.org/10.20965/jdr.2019.p1140>

- Wang Z, Nagashima F, Kawase H (2021) A new empirical method for obtaining horizontal site amplification factors with soil nonlinearity. *Earthquake Eng Struct Dyn* 50(10):2774–2794. <https://doi.org/10.1002/eqe.3471>
- Wessel P, Smith WHF (1998) New, improved version of the generic mapping tools released. *EOS Trans AGU* 79:579

### **Publisher's Note**

Springer Nature remains neutral with regard to jurisdictional claims in published maps and institutional affiliations.

**Submit your manuscript to a SpringerOpen<sup>®</sup> journal and benefit from:**

- ▶ Convenient online submission
- ▶ Rigorous peer review
- ▶ Open access: articles freely available online
- ▶ High visibility within the field
- ▶ Retaining the copyright to your article

---

Submit your next manuscript at ▶ [springeropen.com](https://www.springeropen.com)

---